Design of a Constraint Device for Compliant Bodies using Quasi-Conformal Contact Surfaces as Applied to Mouse Imaging

by

Lucy W. Du
S.B. Mechanical Engineering
Massachusetts Institute of Technology, 2014

Submitted to the Department of Mechanical Engineering
in Partial Fulfillment of the Requirements for the Degree of
Master of Science in Mechanical Engineering
at the
Massachusetts Institute of Technology

June 2016

Signature redacted

Signature of Author.....
Lucy W. Du
Department of Mechanical Engineering
May 20, 2016

Signature redacted

Certified by.....
Martin L. Culpepper
Professor of Mechanical Engineering
Thesis Supervisor

Signature redacted

Accepted by.....
Rohan Abeyaratne
Professor of Mechanical Engineering
Graduate Officer

Design of a Constraint Device for Compliant Bodies using Quasi-Conformal Contact Surfaces as Applied to Mouse Imaging

by

Lucy W. Du

Submitted to the Department of Mechanical Engineering on May 20, 2016
in Partial Fulfillment of the Requirements for the Degree of
Master of Science in Mechanical Engineering

ABSTRACT

The purpose of this work is the modeling and prototyping of quasi-conformal constraint contacts and the investigation of their positioning ability for compliant bodies, specifically for the holding of mice in optical imaging setups. The direct application of this work is the restraint of laboratory mice for biological imaging of micron- and submicron-scale biological structures. No existing research has measured the shear stiffness of mouse facial tissue or modeled the effect of quasi-conformal contact constraints on nonlinear materials. The constraint devices and techniques currently available for mice have limitations that have prevented further exploration of their biological structures. The theoretical model, design rationale, and testing results of a prototype device utilizing quasi-conformal constraints are presented in this thesis. This device is capable of restraining anesthetized mice to sub-micron movement in all axes of translation, without additional surgery or discomfort to the mouse. With the findings presented in this thesis, the design of further optimized devices can be made—both for anesthetized and awake mice—enabling further studies in bone marrow and neural activity that are currently impossible. This could ultimately lead to breakthroughs in stem cell and neurobiological research.

Thesis Supervisor: Martin L. Culpepper
Title: Professor of Mechanical Engineering

ACKNOWLEDGEMENTS

There are truckloads of people that have supported me through this whole "these-ing" process whom I cannot thank enough.

First, I would like to Professor Marty Culpepper, who welcomed me into the Precision Compliant Systems Lab (PCSL) long ago, when I was just a wee-sophomore. I have learned countless invaluable skills—professional, academic, and otherwise—over the last 5 years. Without his guidance and support, I would not have become the engineer that I am today.

Next, I would like to thank the staff at MGH Center for Systems Biology, Professor Charles Lin, and Professor Shih-Chi Chen for their collaboration on this project. Many thanks to Raphael Turcotte for the help in testing and understanding the application and scope of the project. Particularly, I would like to thank Tony Raphael for his help, patience, and time while Rachel and I came over to MGH time after time with various odd requests for mouse testing. He has gone incredibly out of his way to help us with our data collection.

My fellow PCSL labmates (Aaron Ramirez, Marcel Thomas, Charlie Wheeler, and Rachel Dias Carlson) have provided much encouragement and advice over the past several years. Without their guidance and wise words about research, classes and grad life in general, I would still probably be running around in circles with my hair on fire. My time in the PCSL has been amazing with their camaraderie and companionship.

Thanks to all the MakerWorks mentors for their help and advice on design, machining, and much more. I could always count on MakerWorks to be a great place to hang out and learn something new while procrastinating. I have received more guidance from them than I could have ever imagined. Further thanks to the people of LMP, particularly to Bill Buckley and Saana for their support over the years.

I would like to thank all of my friends who listened to my endless months of complaining and dramatizing, while responding only with endless words of encouragement and the occasional sassy comment to put me in my place. Many thanks to Chris Merian and John Mayo for

continuously reminding me to stop overcommitting myself and reminding me to sleep. I don't know what kind of impossible mess I'd be in if it weren't for them.

Next, there's Maha Haji, who has an amazing ability to make me feel sane, even in my most insane moments. She has convinced me day after day that I haven't gone crazy, and that there's always a light at the end of the tunnel. Thank you for making me believe that things will always get better. Oh and for binge-watching "Once Upon a Time" with wings and rose wine. A million thanks to Hanna Lin, Julia Hopkins, and Cynthia Lu for their endless supply of encouraging words and "YOUGOTTHIS" statements. I loved (and desperately needed) every second of our brunches, Dumpling House deliveries, and pretentious hot chocolate sessions. I would also like to thank Cyndia Cao for humoring me and pretending to "be productive" with me while actually watching Disney movies and playing League of Legends (for better or for worse). Finally, thank you to Jamison Go, for inspiring me to be a better engineer and to believe in myself. I would have never achieved as much as I have today without you, and I know you will continue to inspire me to succeed in the future.

Last and definitely not least, I would like to thank my family. Thanks to my parents for raising me, teaching me, and bearing with me through all my grumpiness, panics, and temper tantrums. My sister, Beverly, has been the best role model a little sister could ever have. I have looked up to her my whole life and owe much of my motivation for success to her incredible achievements and encouragements.

CONTENTS

FIGURES

TABLES

CHAPTER 1

INTRODUCTION

The purpose of this work is to model and prototype quasi-conformal constraint contacts and investigate their positioning ability for compliant bodies, specifically for the holding of mice in optical imaging setups. This work includes: the design of a material property testing device for mouse tissue, material property characterization of mouse tissue in compression and shear directions, a modeling method for predicting the stiffness of quasi-conformal constraints, the design of a mouse constraint device utilizing quasi-conformal constraints, and preliminary testing of a prototype. Existing research has not characterized shear properties of mouse tissue; mouse facial muscle material properties has also not been investigated. The constraint devices and techniques currently available for mice have limitations addressed later in this thesis. The techniques and findings presented in this thesis may be used to design other constraint systems using quasi-conformal contacts and nonlinear elastic materials.

The direct application of this work is the restraint of laboratory mice for biological imaging. Currently, the quality of biological images of micron- and submicron-scale biological structures is limited by the movement of the mouse specimen, rather than the resolution of the imaging equipment. A proper restraint device that limits the movement of the imaged mice can enable the full resolution of the imaging equipment to be utilized. With proper images, these biological structures can be better examined and tracked, leading to more significant findings. No prior work has been done to investigate the performance improvement of conformal contacts on the constraint of nonlinear elastic materials. The devices previously designed for similar applications have not been designed following mechanical constraint design rules. With the

findings presented in this thesis, a design of a device can be optimized keeping both predicted performance and user interface in mind.

The prototype restraint device built in this thesis is shown in Figure 1.1. A mouse is placed in the device and prepared for surgery prior to the application of the rear constraint. When the mouse is ready for imaging, the rear quasi-conformal constraint is applied.

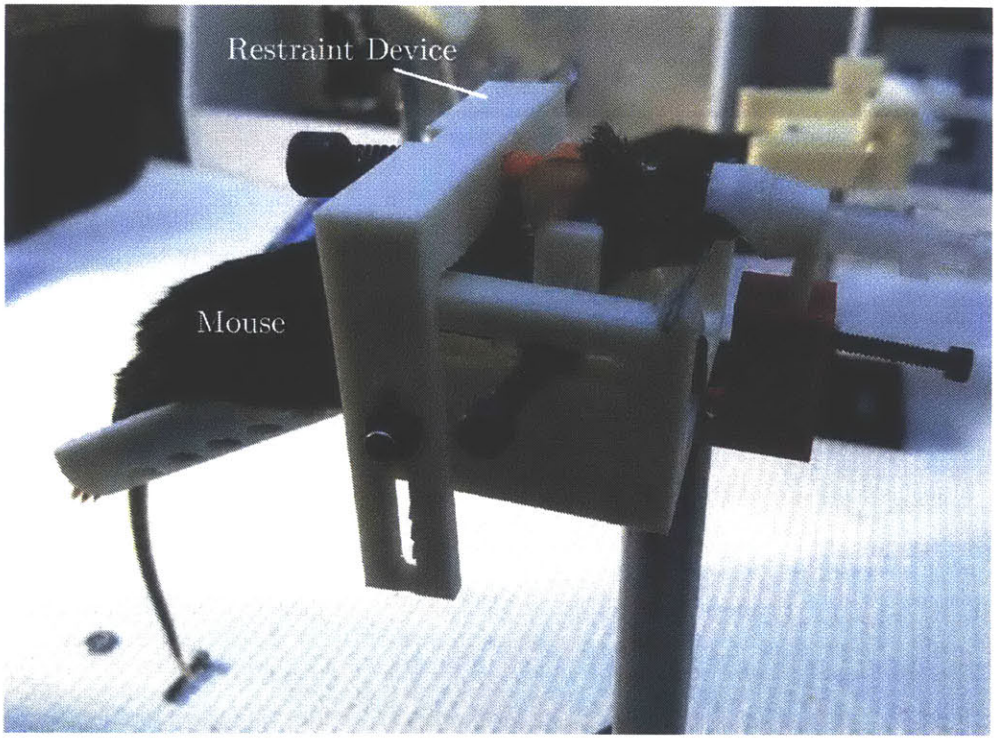

Figure 1.1: Prototype mouse restraint device.

The performance of the device is defined by the magnitude of the mouse movement in three axes. This movement was measured using capacitance probes and a conductive block fixed to the mouse skull. Figure 1.2 shows the displacement of an anesthetized mouse over time during the testing of the prototype device both with and without a quasi-conformal rear constraint. The mouse's breaths and heartbeats can be seen clearly in the movements. The movements of the mouse in the y-axis (lateral) and z-axis (axial) are decreased when using the quasi-conformal constraint, indicating a stiffer and higher performance device.

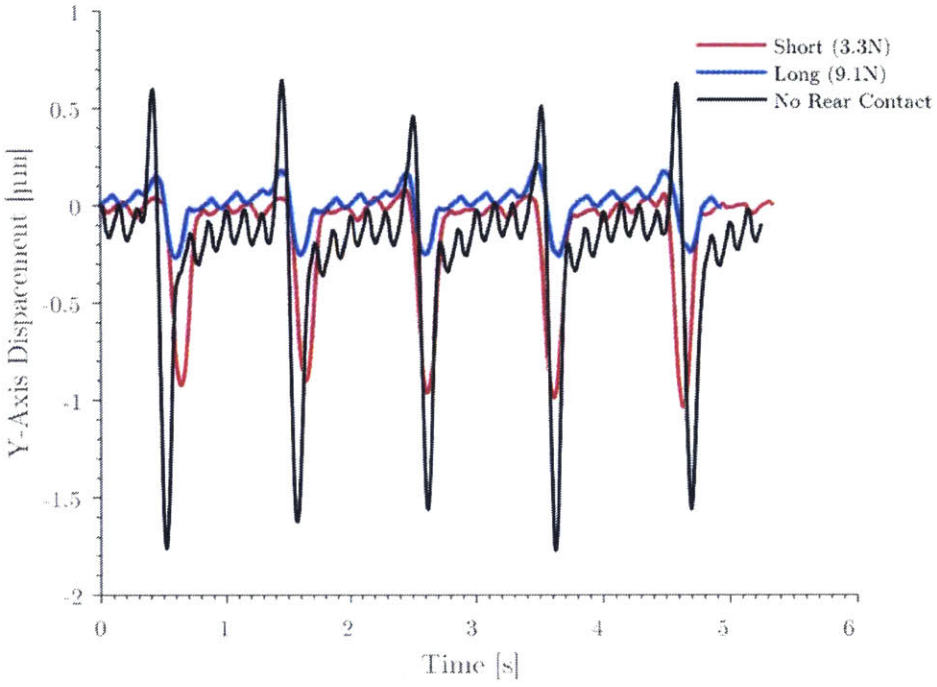

(a)

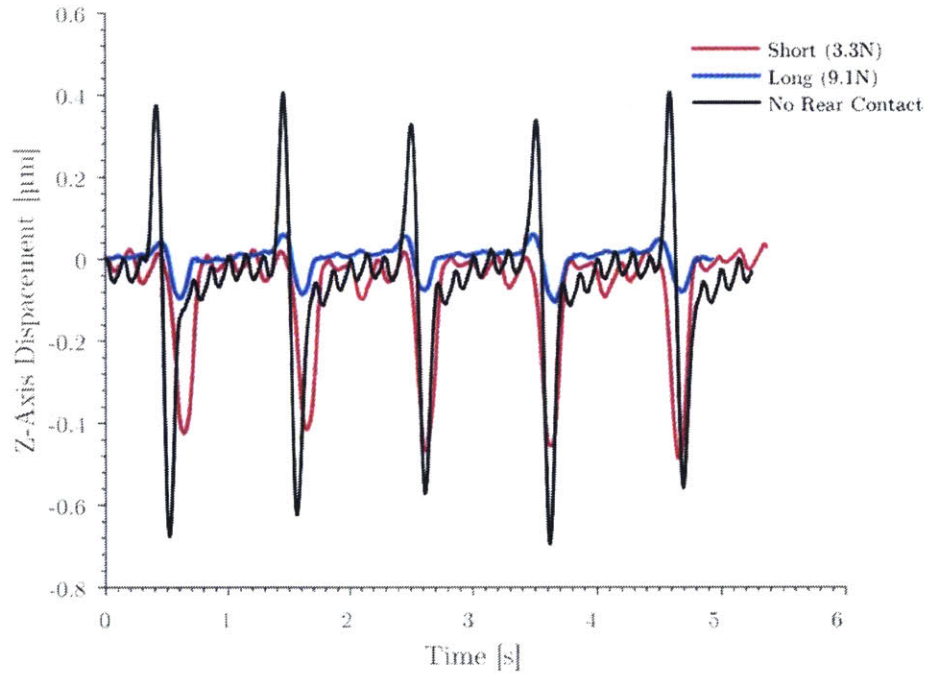

(b)

Figure 1.2: (a) Y- and (b) z-axis mouse movement from testing of prototype device.

1.1 Constraint Devices and Design Principles

Many of the restraint devices that exist today for holding biological specimens were designed empirically rather than using systematic design principles. There are two design principles that are typically used in machine design: kinematic constraint and elastic averaging. Kinematic constraint uses one contact to constrain each degree of freedom of a rigid body. This allows positioning of the body to be highly repeatable and accurate, as there is no forced geometric congruence and no over constraint. One of the limitations of kinematic constraint is the high stress at each point contact and lower overall system stiffness. Elastic averaging uses a large number of contact points to spread out the support of a large load. This type of mechanism is over constrained, but over time and wear, the high and low contact stresses of the points will eventually average out by elastic deformation. An elastically averaged system typically has higher load capacity and stiffness [1]. Two everyday examples of kinematic and elastic averaging are shown in Figure 1.3. The 3-legged stool locates the stool on a surface by exactly constraining each degree of freedom. However, a swivel chair uses more than the necessary number of constraints to distribute the pressure at each constraint location.

(a) (b)

Figure 1.3: The 3-legged stool (a) is an example of kinematic constraint, while a 5-legged rolling chair (b) is an example of elastic averaging [2], [3].

For the application of restraining biological bodies, the requirement for repeatability of placing the specimen in the same location relative to the holder is not necessary. The desired stiffness of the overall system is more important. Additionally, applying a high local contact pressure can be detrimental to the biological subject in the device; distributing the restraint force over a larger area decreases the local contact pressure, which can allow for higher overall restraint forces. Therefore, elastic averaging is the chosen design principle for this prototype device.

1.2 Motivation and Application: Mouse Imaging

In vivo imaging of live animals has resulted in many biomedical and clinical research advancements. Animal biological models provide a platform to study the progression of diseases and therapeutic responses requiring manipulation that cannot be performed directly on humans. The mouse is the most widely used model for the study of human systems. Many of these studies use sub-micron imaging techniques to image tissue and organ structures in order to monitor and characterize physiological activity in animals. The genetics, housing conditions and diet of mice can easily be controlled to achieve the biological conditions required for certain tests and experiments [4]. Imaging techniques and biological structures of interest will be discussed in the sections below.

1.2.1 Background: Optical Imaging

Optical imaging is the most common method used to image tissue structures and features in mice. Two of the most commonly used imaging methods are confocal and two-photon microscopy. A diagram showing the fundamental differences in confocal and two-photon microscopy is shown in Figure 1.4.

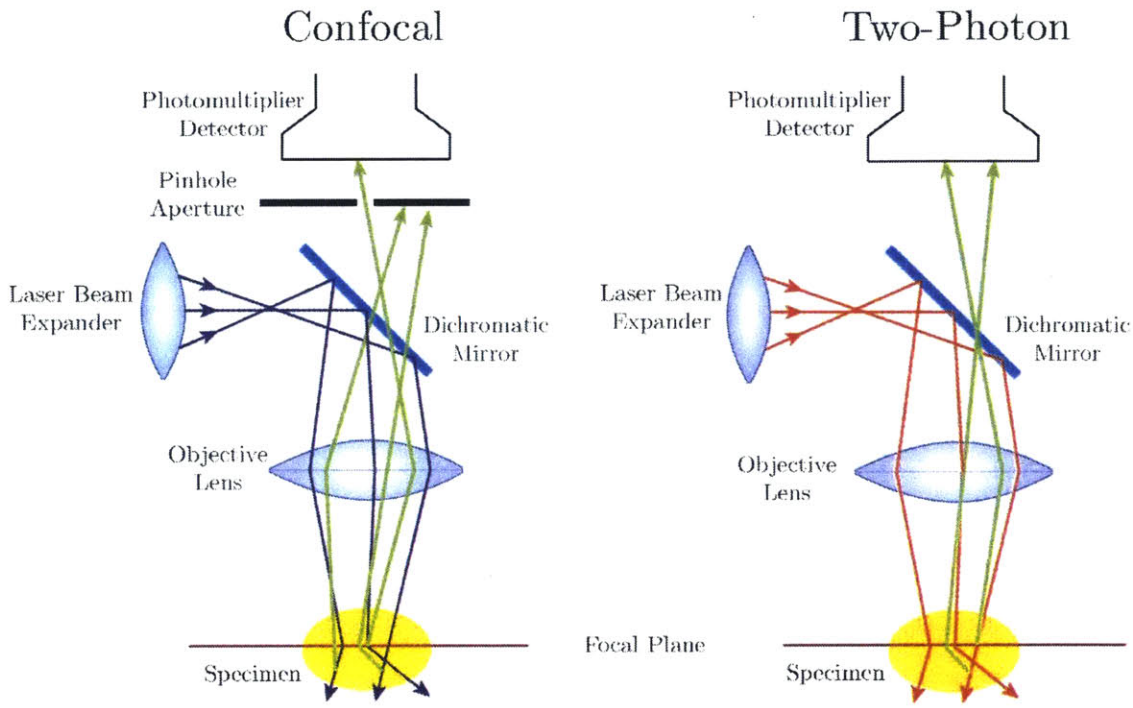

Figure 1.4: Confocal and two-photon microscopy.

A confocal microscope detects either scattered light or fluorescent light from an illuminated specimen. The pinhole aperture then filters out the out-of-focus background fluorescence to produce a clear optical image. However, large excitation volume can cause phototoxicity in cells and compromise the integrity of the entire cell, leading to severe problems in live specimen. Therefore, the overall excitation volume for confocal microscopy should be kept minimal, limiting the effective penetration depth of confocal microscopy [5], [6].

Two-photon microscopy provides an advantage in imaging living cells, especially in the form of intact tissues and organs. The absorption of photons depends on the square of the excitation intensity and for two-photon microscopy, the only location along the optical path crowded enough for two-photon excitation is the focus plane. Above and below the focal point, the density is not high enough for both photons to pass, preventing the phototoxicity problem in confocal microscopy [6]. The resulting image from two-photon microscopy has the same resolution as a confocal microscope.

Other types of imaging techniques used for *in vivo* imaging of specimen are Optical Coherence Tomography (OCT), Adaptive Optics Scanning Laser Ophthalmoscope, Positron Emission Tomography (PET), and Magnetic Resonance Imaging (MRI). The common imaging methods and their resolutions are shown in Table 1.1. The resolutions listed for lateral and axial directions are relative to the objective lens of the microscope.

Table 1.1: Imaging techniques and resolutions.

Imaging Technique	Lateral Resolution	Axial Resolution	Units
Optical Coherence Tomography (OCT) [7]	3	1	μm
Multiphoton Microscopy [8]	0.207	0.814	μm
Adaptive Optics Scanning Laser Ophthalmoscope [9]	0.7	2	μm
Spectral Domain OCT [10], [11]	2.4	1	μm

The imaging performed at the MGH Center for Systems Biology is primarily confocal and two-photon microscopy. While these imaging methods have high resolution, the movement of the live imaging subject does not allow the full use of the high resolution capabilities. Anesthetized subjects simplify this problem for some studies where anesthesia does not affect the structures imaged, but the movements of heartbeats, breaths, and occasional convulsions that range from tens of microns to millimeters can still result in blurry images without proper restraint. There exists post-processing software that can mitigate the effect of mouse movement over long periods of imaging, but these methods are costly and time consuming.

A proper restraint device that can restrain the motion of a mouse during an imaging session of up to 24 hours would allow for: high resolution images micro-tissue structures, tracking of cell movement over long imaging periods, and study of physiological response to sensory input in awake animals. The prototype in this thesis was designed for anesthetized mouse imaging, but the methods developed in this thesis can be applied to designing a holder for awake animals.

While some stereotaxic devices currently exist, many studies find that they are insufficient to achieve the quality of images required, even for anesthetized mice. One study reported that the "movement caused by heartbeat, respiration and slow drifts prevented online improvement of

signal to noise ratio by frame averaging" [12]. It has also been reported that "tissue movement by as little as a few micrometers can render three-dimensional image stacks uninterpretable" [13]. A device designed to properly constrain the movement of mice to less than $1\mu m$ would enable better images and lead to further advancement in clinical and biomedical studies, detailed below.

1.2.2 Bone Marrow Imaging

Bone marrow is an extremely impactful biological structure of interest. Transplantation of bone marrow is crucial to stem cell based therapy and is used to treat cancers of the blood system. The tracking of stem cells during the homing and engraftment process allows researchers to characterize the cell environment, promoting cell survival. Hematopoietic stem cells are usually 12-25μm in size, while capillaries and red blood cells are typically 5-10μm and 6-8μm, respectively. The imaging of the bone marrow in the skull for a 24 hour imaging period is necessary to observe the cell migration and proliferation process for this characterization. An example of stem cell images for bone marrow imaging can be seen in Figure 1.5.

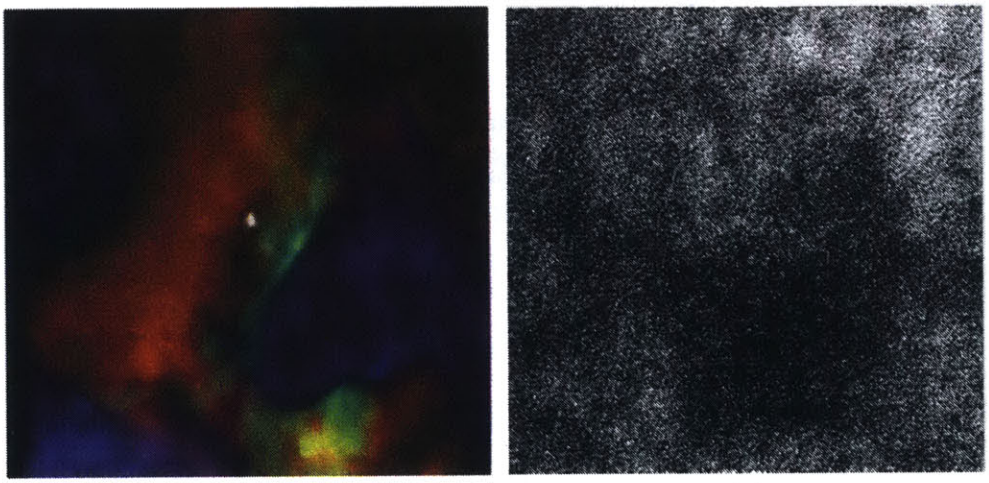

(a) (b)

Figure 1.5: Image from a two-photon microscope (a) with and (b) without a mouse holder [14].

1.2.3 Brain Imaging

In vivo brain imaging is another important direction of interest in the biomedical field. Studying a functional brain enables scientists to map neural circuits and investigate brain function related motor activity. Brain function can be monitored for changes as a result of aging and disease, allowing scientists to study the effects of diseases on brain function and aid in the development of cures [15]. While some of these tests can be performed on anesthetized mice, the anesthesia suppresses some cerebral function, making it difficult for researchers to obtain certain data required to study brain cancer and strokes. There is currently research being done to investigate the use of anti-angiogenic drug therapies to repair vascular network cells destroyed by brain tumors in order to develop more efficient therapies [16]. The structures of interest in the brain are neurons and dendrites that range between $0.2\mu m$ and $2\mu m$ in size. A device to constrain mice, particularly awake and un-anesthetized, without pain or discomfort would allow these studies to progress further. Figure 1.6 below shows an example of brain imaging taken for anesthetized mice.

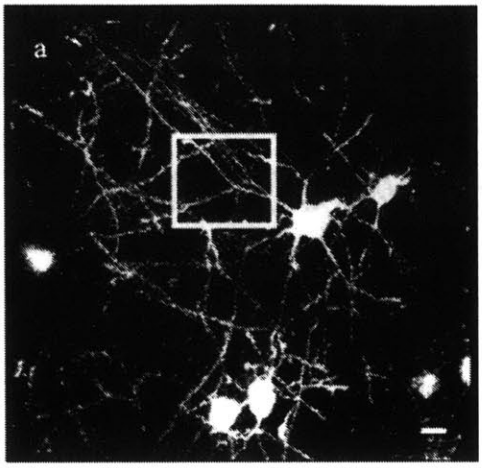

Figure 1.6: *In vivo* imaging of dendrites and dendritic spines. Scale bar: $10\mu m$ [12].

1.3 Prior Art: Holding Devices and Methods

There currently exists several devices and methods used to restrict movement of mice for various biological imaging setups and surgeries. This section introduces these restraint methods along with their limitations and discusses the motivation and necessity of a new device.

1.3.1 Positioning Ability

The positioning ability of some existing constraint methods are shown in Figure 1.7; the relative maximum resultant movements of these methods and setup times are shown. Some of these methods require surgery and permanent adhesion of parts to the skull of the mouse, while others use adjustable probes placed around the mouse's head for positioning. The limitations to adhesion methods is discussed in Section 1.3.2. None of the current methods are able to restrain the movement of mice to less than $1\mu m$, the desired maximum displacement for highest quality images. To best utilize the high resolution imaging equipment that exists today, the restraint device would need to constrain the mouse such that the maximum movement is less than the resolution in each direction. For most imaging methods, the maximum allowable movement is $1\mu m$.

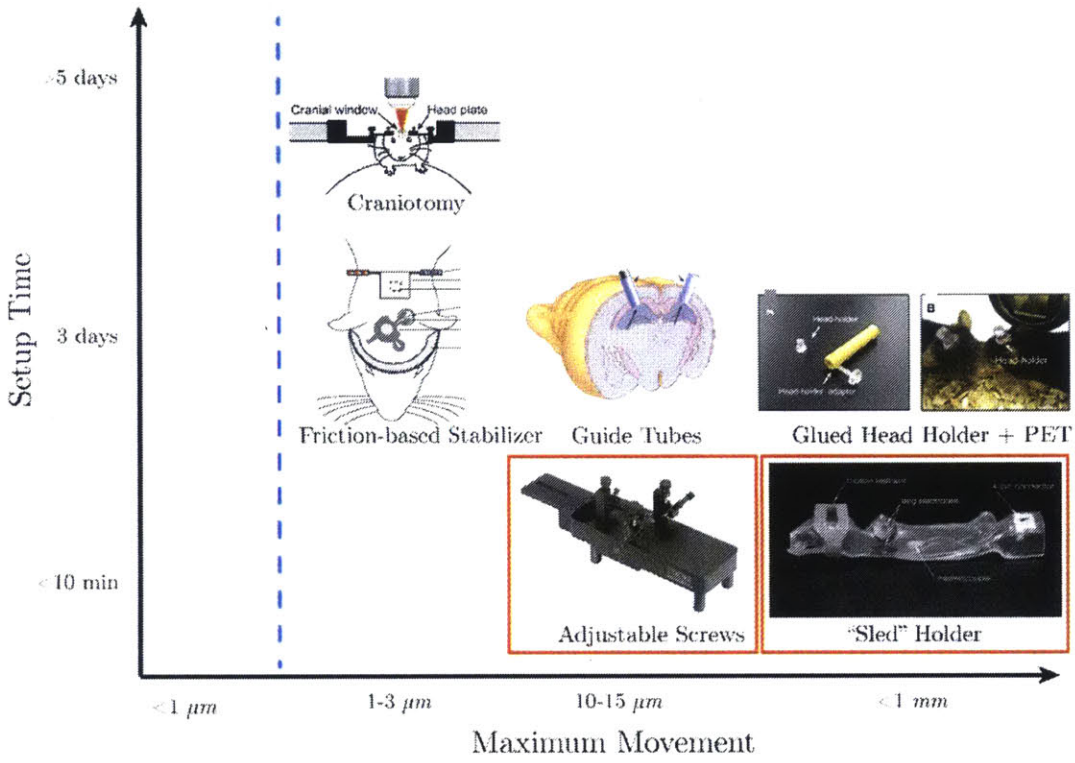

Figure 1.7: Restraint techniques compared against setup time and performance [17]–[21].

Reproduced with permission. All rights reserved. License #3782610888279, 3782611041718, 3866080040041.

The design of most of these methods were developed through trial and error, rather than a systematic design progression. A mouse restraint device for anesthetized mice was developed by Culpepper *et al* [22]. This device utilizes the principle of exact kinematic constraint with three contact points on the mouse's head, and a bite bar. These points exactly constrain all six degrees of freedom of the rigid body (mouse head). The prototype is shown in Figure 1.8.

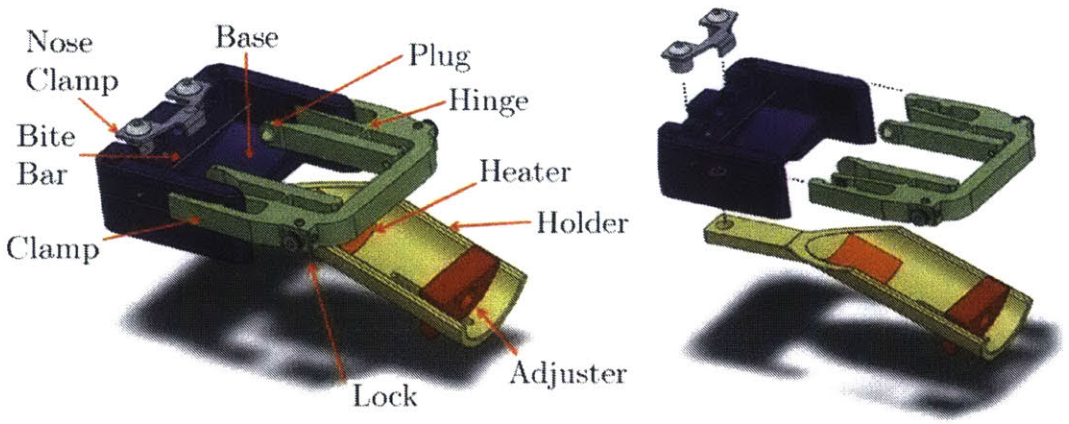

Figure 1.8: Prototype mouse holder designed by Culpepper *et al* [22].

The performance of this device was measured using capacitance probes, and the device was able to keep maximum skull movement to 0.1-0.2μm for heartbeats. A mouse was allowed to wake up from the anesthesia to test the performance of the device for awake mice, but the device was unable to restrain the mouse to $<1\mu m$. The data collected from these tests are shown in Figure 1.9.

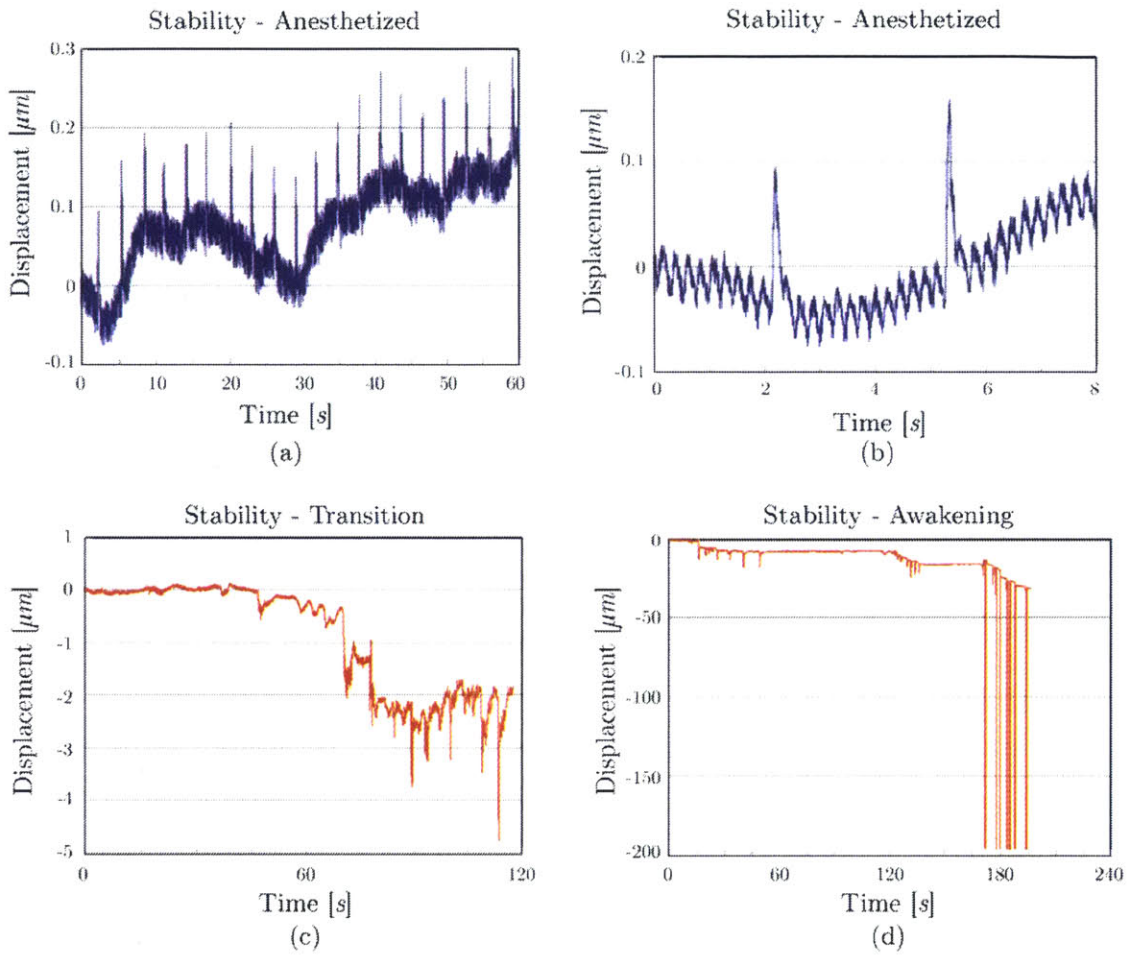

Figure 1.9: Measured displacement of initial prototype device of an anesthetized mouse over (a) 60s, (b) 8s, (c) during transition from anesthetized to awake and (d) fully awake [22].

While this initial prototype was able to restrain anesthetized mice to $<1\mu m$, more design modifications would need to be made for awake mouse imaging without rigidly adhering any parts to the skull. The effectiveness of elastic averaging was explored for the development of the prototype in this thesis.

1.3.2 Invasiveness

The devices shown in Figure 1.7 have varying degrees of invasiveness. Some of the more invasive methods involve performing surgery on the mouse to attach a plate permanently to the

skull. This plate is then bolted down firmly to a rigid test setup under the microscope. This method requires time for surgery, but also several weeks of recovery time for the mouse to adjust to the attachment plate. This method is able to achieve the best performance, but has one major limitation in addition to the surgery and setup time. The rigid attachment of the plate to the skull requires adhesives, which are toxic to the cells in bone marrow; this method cannot be used for bone marrow imaging. The device proposed in this thesis aims to be minimally invasive such that no extra setup time besides placing the mouse in the holder is involved.

1.3.3 User Interface

The design for a restraint device not only needs to fulfill the functional requirements, but also needs to be easily usable for the biologists acquiring the images. If the device is not easy to use, the time spent to use the device could be spent on post-processing images, or further surgery for cranial windows instead. It is also important for biologists to have haptic feedback when they apply the contacts on the mouse, so that they can feel how hard the contacts are pushing on the mouse. All adjusting screws need to be easily graspable by an adult hand, as the use of further tools (screwdrivers, wrenches, etc.) would be an extreme hassle.

Another consideration is the space and form factor of the restraint device relative to the imaging setup. All optical setups would require direct access to the top of the head and require some clearance around the location. Therefore, any parts above the plane of imaging on the head could interfere with the objective lens or any part of the microscope. Figure 1.10 shows locations on a mouse's head that need to remain accessible to biologists and cannot have portions of the device in the way.

Figure 1.10: Locations on a mouse head that must remain clear for device design (shown in red) [23].

1.4 Thesis Outline

Chapter 2 of this thesis presents the design of experiment and experimental results for the characterization of mouse facial tissue. Chapter 3 discusses the theoretical modeling of the quasi-conformal contacts and how to incorporate them into a holistic model of a holder system. A detailed design process utilizing the data and calculations from Chapters 2 and 3 is discussed in Chapter 4 for a prototype holder optimized for data collection and testing. Chapter 5 details the experimental design, setup, limitations, and data acquisition process for the holder. The results of the experiment and overall performance of the holder are also discussed. This thesis concludes with a synopsis of the work, results, and a discussion of future work in Chapter 6.

CHAPTER

2

MOUSE TISSUE CHARACTERIZATION

This chapter presents the method used to determine and characterize the compression and shear stiffnesses of mouse tissue. Section 2.1 describes the motivation and importance of the material properties to be measured. The design of the materials testing device is presented in Section 2.2, and the setup and measurement procedures are defined in Section 2.3. The results and analysis are discussed in Section 2.4.

2.1 Measurement of Material Properties

When designing a positioning device for compliant objects, the stiffness of the compliant object contributes a large factor to the compliance of the overall system. It is crucial to understand the material properties of the compliant object in question, in this case, mouse facial tissue. The tissue on top of the bone consists of a layer of skin above a layer of muscle. This contact joint can then be modeled as springs in series, as shown in Figure 2.1.

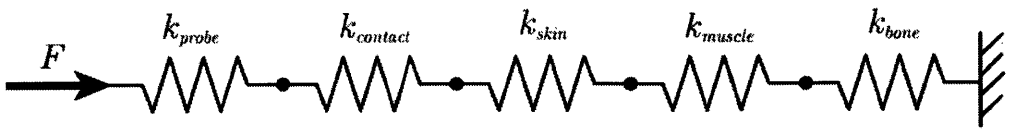

Figure 2.1: Contact joint spring model.

Skin, like many materials, has different properties in tension and compression. The tensile modulus of mouse skin was found to be $6MPa$ at 20-30% strain, while the compression modulus was only $32kPa$ at the same strain [24]. Based on these findings, a device that could hold the skin of the mouse in tension, rather than compression for position could allow for a stiffer device. However, pulling the skin in tension may cause discomfort, pain, and injury for the mouse. The most practical strategy is to hold the mouse with contact points that apply compression on the skin.

Figure 2.2 below shows a contact pushing on the skin of a mouse. The contact probe compressing the tissue would apply a force, $F_{contact}$. The mouse being held could apply forces either axial to the contact probe—indicated by F_{mouse} (1)—or perpendicular to the contact probe—indicated by F_{mouse} (2). The stiffness of the overall contact joint is determined by the compression stiffness of the relevant materials for movements in the axial direction (relative to the contact probe) and the shear stiffness for movements in the perpendicular direction.

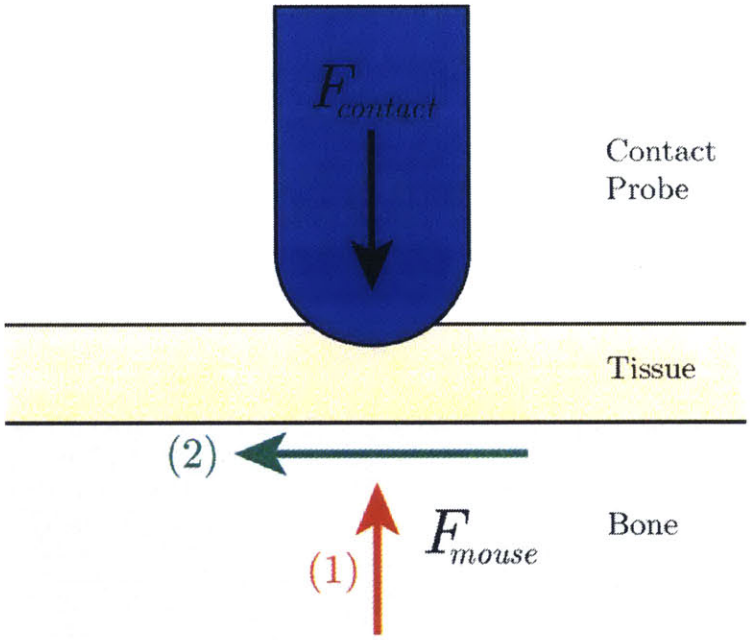

Figure 2.2: Applicable forces in a contact constraint system.

2.1.1 Tissue Material Behavior

The tissue layer for a mouse is made of skin and muscle both of which are considered nonlinear viscoelastic materials, meaning their stiffnesses change as a function of strain and strain rate. The stiffnesses of the tissues at each contact probe location determine the overall performance of the device. The applied force or strain rate applied to each contact probe directly affects the performance of the device. A typical nonlinear stress-strain curve is described in Equation (2.1).

$$\sigma = \sigma_T(e^{q\varepsilon} - 1), \tag{2.1}$$

where σ_T is the threshold stress and q is the modulus coefficient for the given material. The threshold stress relationship is presented in Equation (2.2).

$$\sigma_T = \frac{F_T}{A}, \tag{2.2}$$

where F_T is defined as the minimum threshold force said to be significant for tissue resistance, and A is the cross-sectional area of the material in compression. A threshold force value of $0.01N$ was used for measurements in both this thesis and the experiments performed by Wang *et al.* An example of a nonlinear stress-strain curve is shown in Figure 2.3.

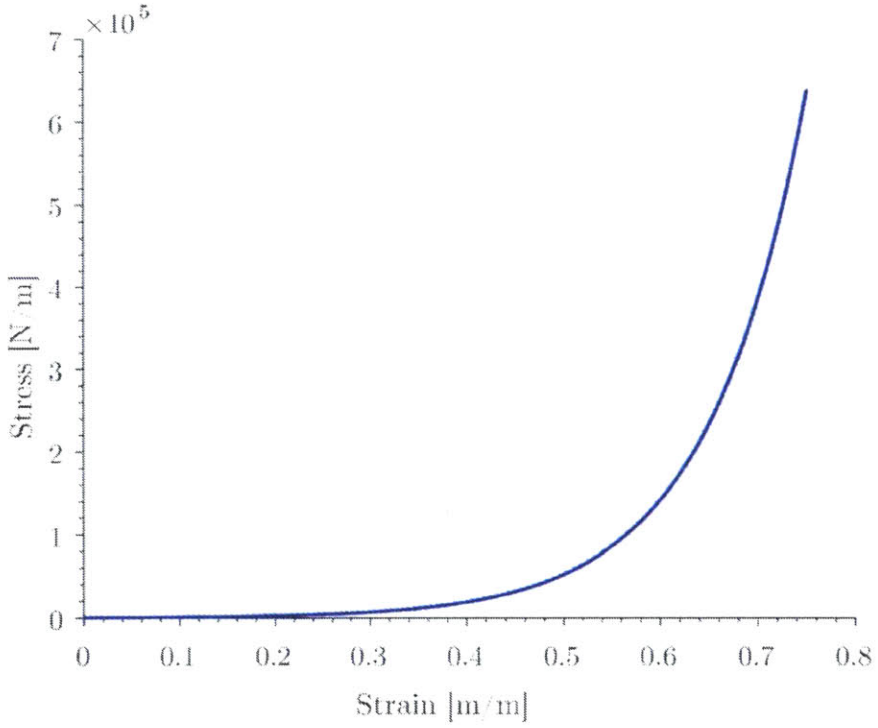

Figure 2.3: Example of a nonlinear stress-strain curve.

To find the elastic modulus, E, of a nonlinear material for a given stress or strain, the localized slope of the stress-strain curve can be found about that stress or strain.

$$E = \left.\frac{\partial\sigma}{\partial\varepsilon}\right|_{\varepsilon} \tag{2.3}$$

The Kelvin-Voigt viscoelastic model states that given a constant applied stress, the viscoelastic material will approach the displacement for a pure elastic material. The strain of the

material under constant stress is shown in Equation (2.4). This phenomenon is known as stress relaxation.

$$\varepsilon(t) = \frac{\sigma_o}{E}\left(1 - e^{-\lambda t}\right), \tag{2.4}$$

where λ is the rate of relaxation, and η is the viscosity of the material. For this device, the contact probe will apply either a constant force or displacement on the tissue. In the case of a constant applied force, the skin may exhibit creep, but will still approach the overall displacement for a pure elastic material. If a constant displacement is applied, the skin may experience stress relaxation, but the final displacement will still be that of the initial application and will not change. Therefore on the operating timescale of this device, viscoelastic effects may be neglected, and the tissue will be considered a nonlinear elastic material.

2.1.2 Material Properties from Literature

The compression modulus and thickness of mouse skin on the hind limb was measured by Wang *et al*, but no measurements have been taken beyond a stress of $71kPa$, and facial skin was not tested. The thickness of skin was found to be $278 \pm 102\ \mu m$ [4]. Further experimentation to measure these values was therefore unnecessary for the proper design of a constraint device. The values measured in this thesis will then be compared with the values published in literature.

The elastic properties of muscle tissue have been characterized by several studies. A study performed by Kot *et al* utilized shear wave ultrasound elastography to find the elastic modulus of human muscle. The values were found to range from $8kPa$ to $46kPa$; however the induced strain during measurement was not stated [25]. Another study utilized ultrasound elasticity measurements to measure the properties of bovine muscle, but strains greater than 0.16 were not induced [26]. Material properties for mouse muscle also need to be known to obtain reliable stiffness values for this thesis.

Both elastic properties and yield strength of mouse bone are necessary to know for the design of this device. These properties dictate the maximum applicable force from each contact,

as well as how the bone material should be treated in the spring system presented in Figure 2.1. One study used three-point bending tests to investigate the properties of an adult rat skull. The elastic modulus of the skull bone at slow loading conditions was found to be $5.917 GPa$ with a standard deviation of $0.763 GPa$. The yield stress of bone was reported to be 104-121MPa [27]. Based on these values, the maximum force that can be applied to the skull based on bone material properties and geometry is $5N$.

In order to model and design a device for this application, the material properties—namely compression, shear modulus, and thickness—for muscle and skin must be known. As a result, a test setup to measure the material properties of mouse facial tissue was designed and built.

2.2 Design of Material Testing Device

The material testing for this application is best performed on a mouse post-mortem. Due to the restrictions of CAC protocols, it would not be practical to place the mouse in a Universal Testing Machine, such as Instron. A custom test device capable of measuring to the required accuracy and resolution was designed, built, and used. This device was designed and tested in conjunction with Rachel Dias Carlson [28].

2.2.1 Functional Requirements

In order to get a good measurement of the stiffnesses required—compression and shear—the measurement device required a high degree of accuracy and resolution for both input control and output measurements. The functional requirements for this device are outline below in Table 2.1.

Table 2.1: Functional requirements for material testing device.

Property	Required Value	Desired Value	Units
Maximum Axial Force	5	5	N
Shear Direction Travel	10	20	mm
Force Control Accuracy	$\pm$ 0.05	$\pm$ 0.01	N
Dimensional Stability	<1	<1	μm
Displacement Resolution	<100	10	nm
Constant Strain Rate	$\pm$ 0.5	$\pm$ 0.1	mm/s

The *maximum axial force* is the maximum compression force that the chosen actuator would need to apply into the mouse skull. A calculation of the yield strength and measurement of bone thickness of the skull determined a maximum force that is to be applied by the contact probe. *Shear direction travel* describes the required travel of the linear stage in the direction perpendicular to the applied compression load. This linear stage is required to test the shear properties of the skin under compression. The *force control accuracy* describes the maximum allowable error for the magnitude of the input force. The *dimensional stability* refers to the position of the machine components relative to each other for the duration of the test (about one minute). *Displacement resolution* is the smallest measurable increment that could be measured in each axis of interest (x- and y-axes). The *strain rate* applied to the tissue must be constant, so that the viscoelastic effect of the skin does not affect the measurements during the experiment.

2.2.2 Mechanical Design

A single device was designed to do measurements for both compression and shear force-displacement measurements. The completed device is shown below in Figure 2.4.

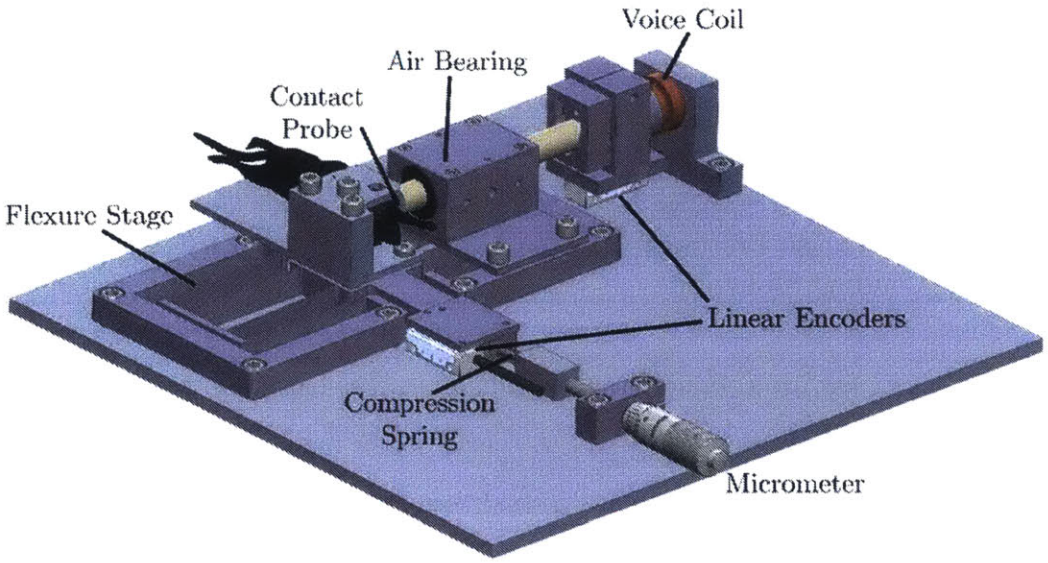

Figure 2.4: Materials testing device setup.

In order to measure the compression modulus on facial tissue of the mouse, an accurate displacement measurement would need to be measured as an incrementally increasing force is applied. For the shear modulus, the actuator would need to apply a constant force as a second perpendicular force is applied. The resultant displacement in the y-direction would need to be measured. Given these constraints, it was necessary to have a force-controlled actuator in the x- and y-axes and accurate, high-resolution displacement measurements in each axis. It is important to note that while the x-direction force actuation must be continuous and actively controlled, the y-direction force application need only be incremental. Figure 2.5 below shows a mouse head with the desired force-displacement inputs and measurements for both compression and shear testing.

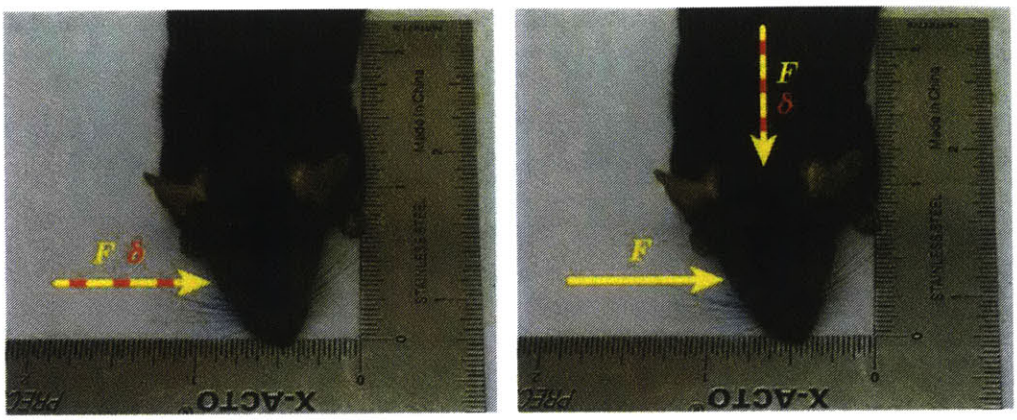

(a) (b)

Figure 2.5: Desired force-displacement inputs and output measurements for (a) compression stiffness and (b) shear stiffness. Inputs are in yellow and output measurements are in red.

2.2.2.1 Linear Stage Design

In order to get accurate force-displacement measurements at the required resolution, all unknown quantities, such as friction, must be eliminated. The compression test only requires movement in one axis, while the shear test requires two. This test setup was thus designed with two frictionless axes of movement, shown in Figure 2.6.

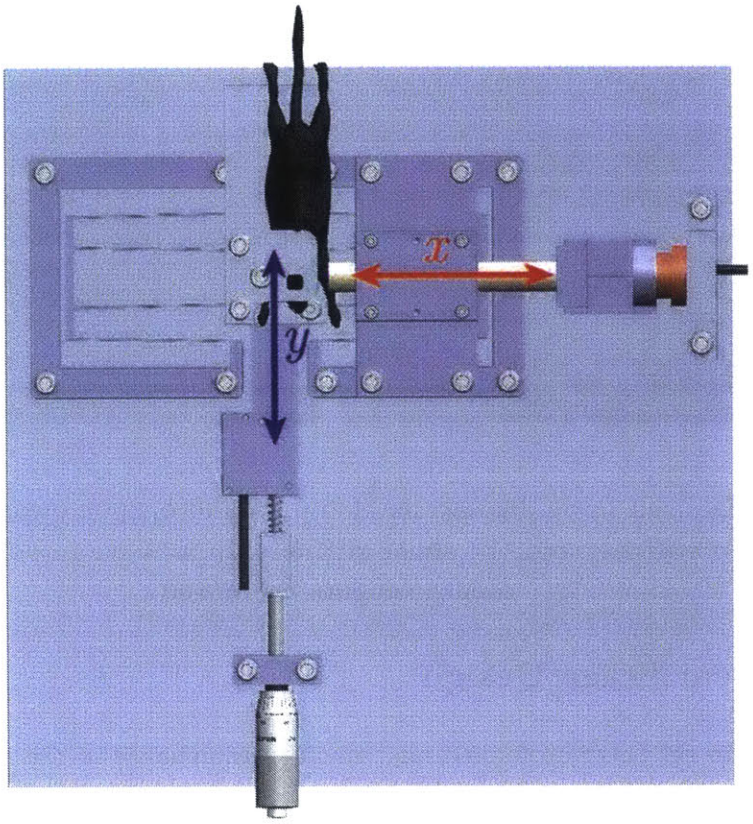

Figure 2.6: Test device top view showing axes of movement.

The mouse is mounted on the center of a symmetrical, single degree-of-freedom, four-bar flexure stage oriented such that the movement of the flexure stage is in the y-direction. The y-axis movement stage components are highlighted in Figure 2.7. A flexure stage was chosen because the force-displacement characteristics of the stage were both repeatable and easily characterized on an Instron. A flexure stage also provides a manufacturable and inexpensive frictionless solution to linear movement at this size scale.

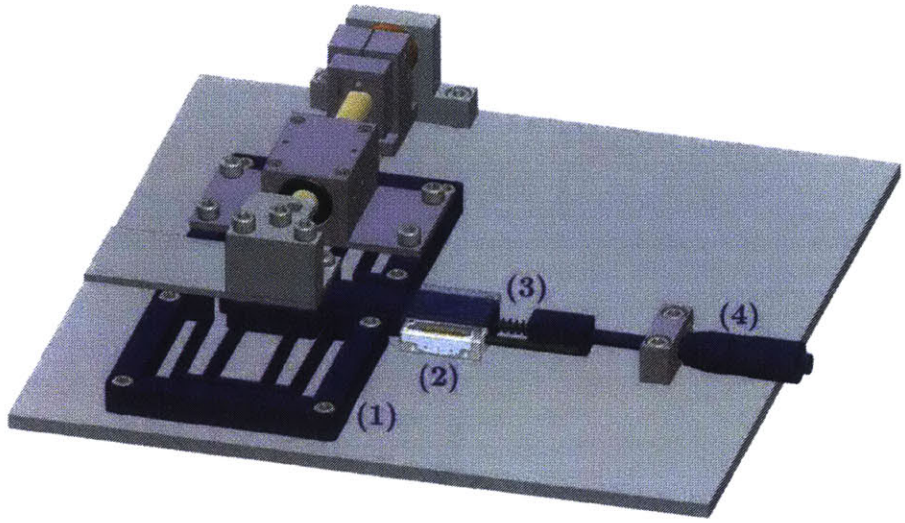

Figure 2.7: Y-axis movement stage components including (1) flexure stage, (2) Renishaw linear encoder, (3) compression spring, and (4) micrometer.

The flexure was optimized according to the functional requirements for force and travel in the x- and y-directions. A safety factor of 2 was applied for yield at a displacement of $3mm$ on either side of the initial position. The geometry of the flexures were designed such that the stiffness in the undesired directions—x and z—were greater than $5 \times 10^6 N/m$. The flexure stage was then characterized using an Instron to account for manufacturing tolerances and errors and confirm the modeling.

The x-axis movement stage was also designed to be frictionless. The 3D printed ABS part contacting the mouse was attached to the end of a precision steel shaft supported by a New Way 0.5" ID air bushing (S301201). The air bearing selected has a radial stiffness of $11N/\mu m$, which is more than sufficient for the radial loads that it would be experiencing [29]. Two Renishaw Linear Encoders (T1001-10A with Ti2000A10A interfaces) were attached to the moving portions of the assembly: one to measure the x-axis displacement of the precision shaft, and one to measure the y-axis displacement of the flexure stage [30].

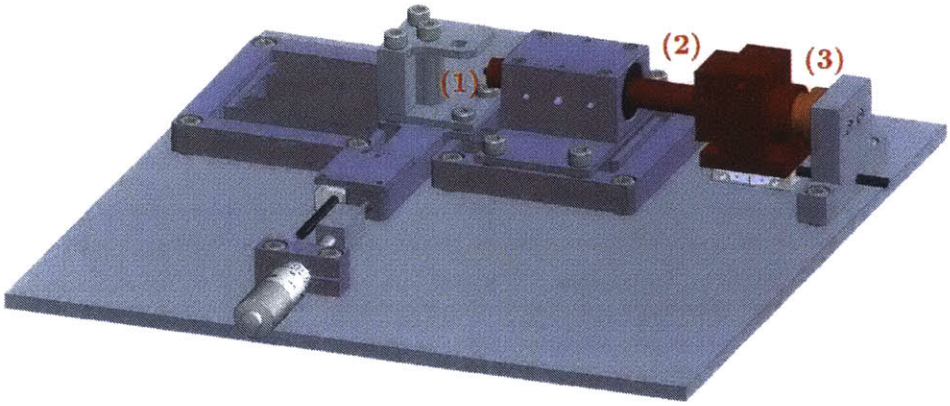

Figure 2.8: X-axis movement components including (1) ABS contact probe, (2) precision shaft in air bearing and (3) linear voice coil actuator.

2.2.2.2 Actuator Selection

The test device has force inputs for both the x- and y-axes, but only the x-direction input force needs to be continuous. Therefore, for simplicity, only the x-axis was chosen to be electrically powered and controlled. Ultimately, a $5N$ Moticont linear voice coil actuator (LVCM-025-029-01) controlled by a LabVIEW program was selected to apply the input force in the x-direction [31]. A linear voice coil was chosen for this application because it provided a simple force-control option through current control and was able to achieve the linear travel and applied force required. The force and corresponding displacements from the Renishaw encoder were then used to determine a compression stiffness of the facial tissue.

For the shear stiffness, the y-axis stage was manually adjusted using a micrometer attached to a compression spring with a known stiffness. The spring constant of the compression spring was characterized previously on an Instron machine. The overall stiffness of the system can be modeled as a system of springs shown in Figure 2.9.

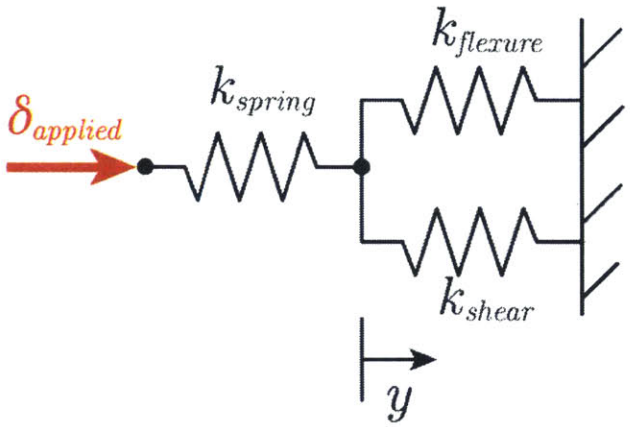

Figure 2.9: Shear stiffness test spring schematic and load path.

When an input displacement $\delta_{applied}$ is applied, the displacement y is measured by a linear encoder. The spring constants of the compression spring ($6.90\ N/mm$) and flexure ($3.16\ N/mm$) were measured individually using an Instron machine. Given these stiffnesses, the shear stiffness of the skin can be calculated and a modulus determined using Equation (2.6) below.

$$\Sigma F = k_{spring}(\delta - y) - (k_{flexure} + k_{shear})y = 0 \tag{2.5}$$

$$k_{shear} = \frac{k_{spring}(\delta - y) - k_{flexure}y}{y} \tag{2.6}$$

2.2.2.3 Sensors and Control

The linear encoders and voice coil were all controlled using a National Instruments DAQ system and a myRIO, respectively. Two LabVIEW programs were written: one to record the linear encoder data and one for force control of the voice coil. The linear encoders have an accuracy of $30nm$ and resolution of $10nm$, and the voice coil can control force within $0.02N$. The electronics schematic and current control schematic are described in detail in Appendix A.

2.2.2.4 Functional Requirements Revisited

The functional requirements for this device are revisited and compared to the values the device has been designed to reach in Table 2.2 below. The error budget and other details for determining the designed metrics are presented in Appendix B.

Table 2.2: Functional requirements & expected performance.

Property	Required Value	*Designed Value*	Units
Force Control Accuracy	± 0.05	*± 0.02*	*N*
Dimensional Stability	<1.0	*2.6*	*μm*
Displacement Resolution	<100	*30*	*nm*
Constant Strain Rate	± 0.5	*± 0.1*	*mm/s*

The dimensional stability required value was not met in the design of this device due to thermal expansion. The temperature of the testing environment was unpredictable. Ultimately, a thermal regulation box made from temperature insulating foam, 80-20, and polycarbonate was constructed and placed around the setup to minimize immediate temperature changes of the setup and minimize expansion for the duration of the test. The thermal regulation box is shown in Figure 2.10.

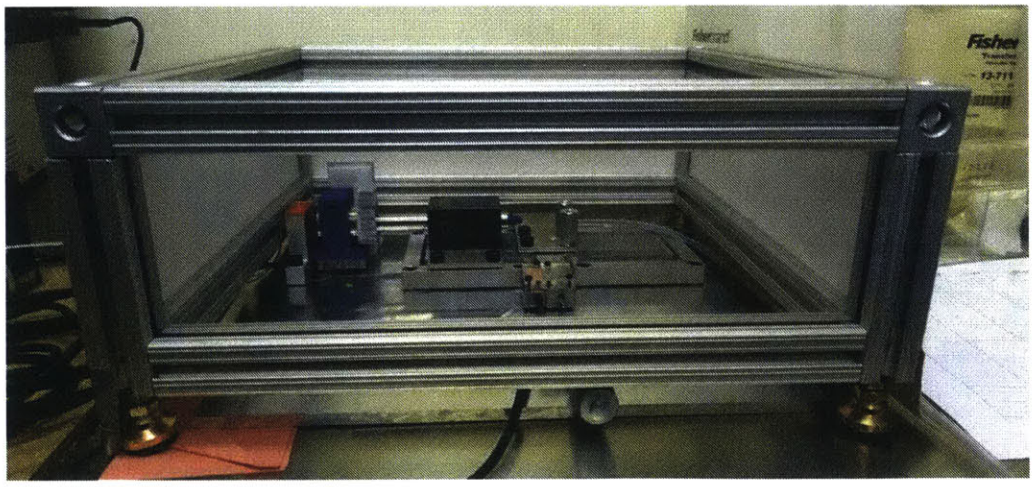

Figure 2.10: Thermal regulation box.

2.3 Experimental Setup and Procedure

The material testing experiments were performed in the MGH Center for Systems Biology with post-mortem type CX3CR1-GFP mice. All testing was performed in accordance with CAC protocols. The masses of the mice tested ranged from 24.1-35g, and ages ranged from 10-14 months. The overall test setup with a fully mounted mouse is shown in Figure 2.11.

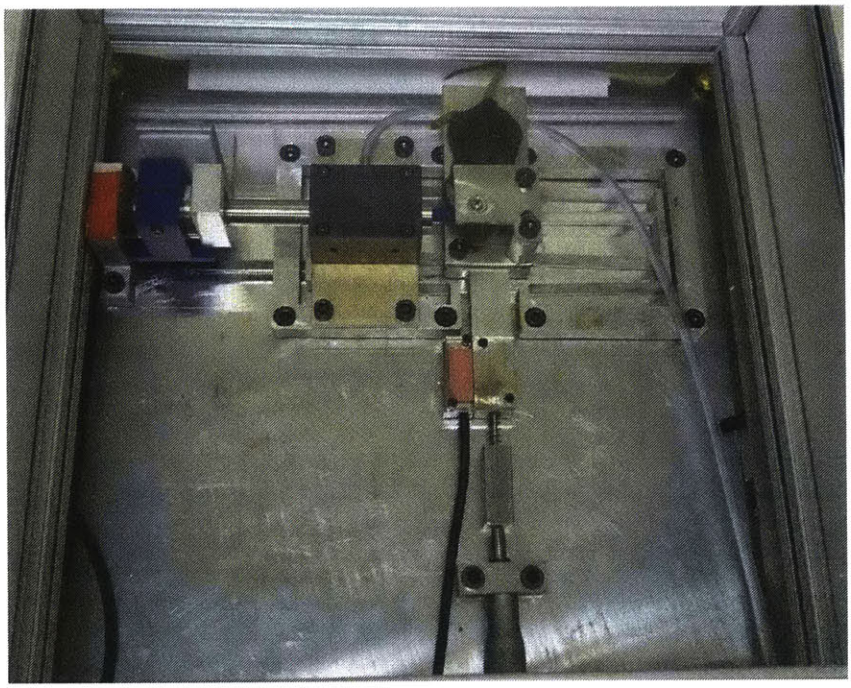

Figure 2.11: Overall material testing setup.

The mouse preparation involved removing the skin and hair on the top of the head to expose the bone of the skull. The skull was then fixed to an aluminum head-plate using dental cement. The head-plate was then bolted to standoffs on the center stage of the flexure.

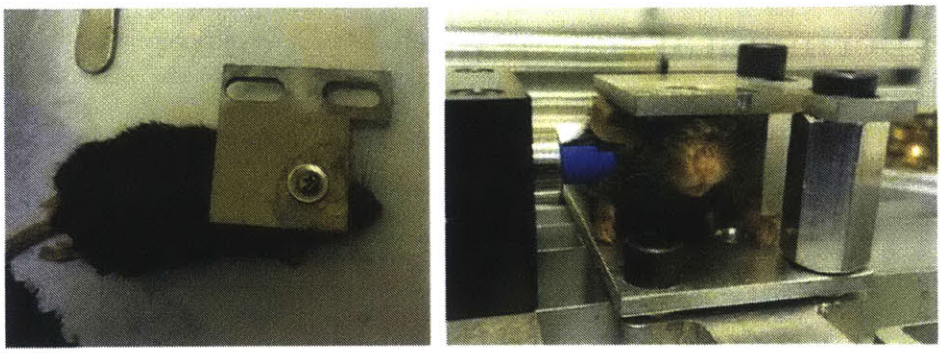

(a) (b)

Figure 2.12: Mouse (a) with bolt in skull and (b) mounted in test device.

After the first trials, it became apparent that the adhesion between the dental cement and the bone was not strong enough to fix the mouse's head. In addition to the adhesive, a bolt screwed into the mouse's head was needed to fix the head relative to the plate for the shear stiffness testing, shown in Figure 2.12. In the testing for the compression stiffness, the 3D printed contact was creating a moment about the attachment point and the head was pivoting about that point. Instead, a separate test where a portion of skin from the mouse's face was removed and placed on an aluminum block rigidly attached to the setup was performed.

2.3.1 Compression Stiffness

According to literature, skin is known to be a nonlinear elastic material. To determine a compression stiffness curve, the displacement is measured as a function of the input force applied by the voice coil. The procedure is outlined below.

1. Remove tissue of interest from the cheek of a mouse.
2. Place the tissue on the setup against the aluminum block (see Figure 2.13). The 3D printed contact is considered touching the skin at $F_{VCA} = 0.01\,N$. The thickness of the tissue at this preload is considered the nominal, uncompressed thickness.
3. Ramp up F_{VCA} at a rate of $0.083\,N/s$ and record the displacement of the voice coil rail.

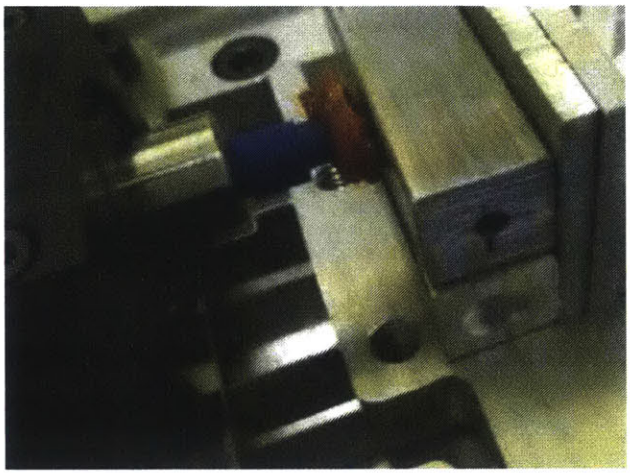

Figure 2.13: Mouse tissue compression test setup.

In addition to the data collected from the test device, further samples were tested on an Instron machine. The setup is shown in Figure 2.14. The tissue samples tested were $6mm$ diameter round samples, and a strain rate of $1\ mm/min$ was applied. As before, the threshold initial force was $0.01N$.

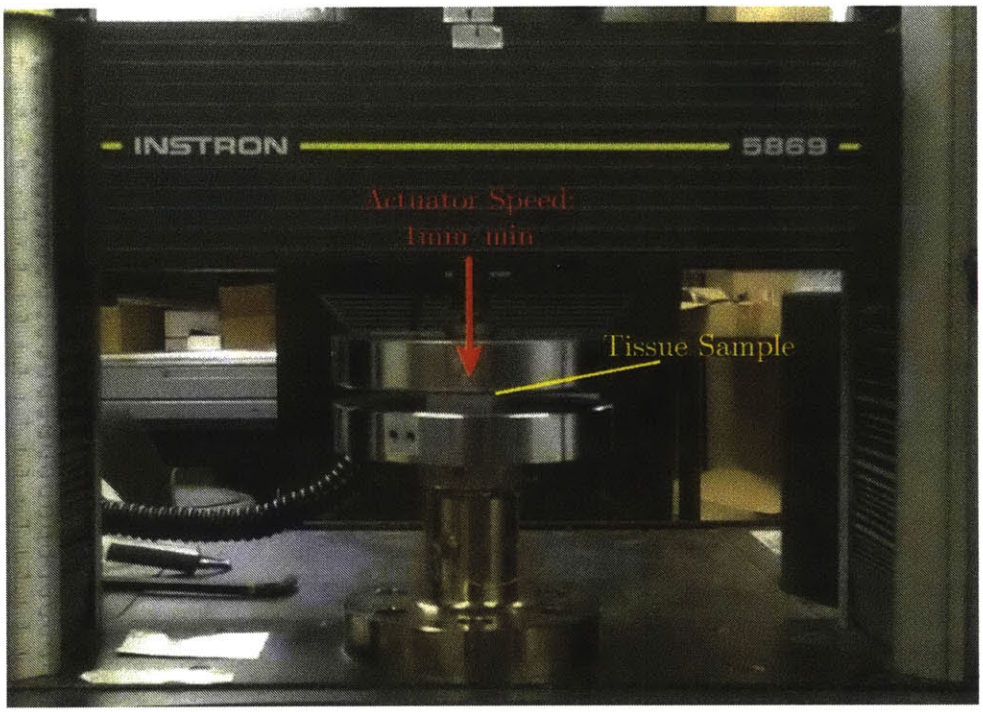

Figure 2.14: Instron setup with tissue sample.

2.3.2 Shear Stiffness

The shear stiffness was measured on the mouse head as a whole. After the mouse is bolted and fixtured onto the test setup, a constant force of $5N$ was applied by the voice coil into the cheek to compress the tissue, as a point-contact constraint would. The experimental procedure is outlined below.

1. Place mouse on flexure stage at the correct height, such that the voice coil probe is between the eye and ear of the mouse.
2. Apply constant $5N$ force with voice coil (F_1) and start recording data from y-axis linear encoder.
3. Turn micrometer in y-direction to apply a resultant force (F_2) on mouse through the compression spring (see Figure 2.15).
4. Incrementally increase the micrometer displacement while continuously recording the resultant y-displacement (δ_y).

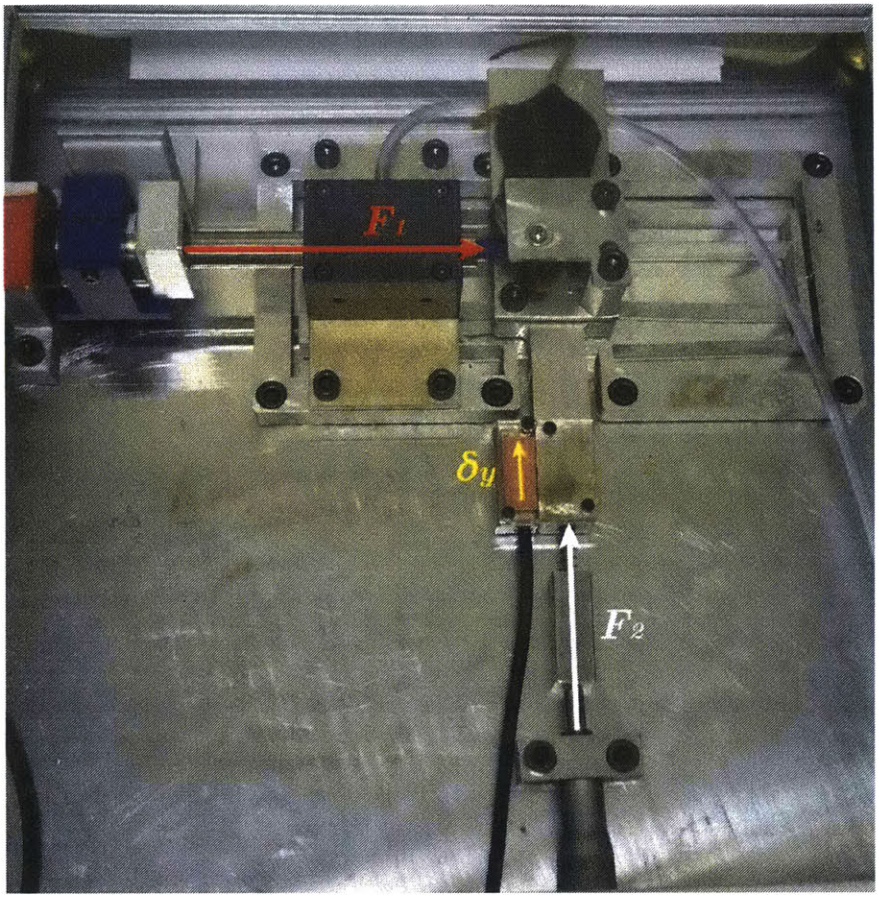

Figure 2.15: Shear stiffness test setup with indicated movement.

2.4 Experimental Results and Analysis

The results from the compression stiffness tests are discussed and compared to similar tests in literature in Section 2.4.1. The results from the shear stiffness tests are similarly discussed in Section 2.4.2.

2.4.1 Compression Stiffness

The force-displacement data was collected for 12 tissue samples from a variety of possible holder-contact locations on the mouse. Each curve was fit using Equation (2.7), where $F_T = 0.01\ N$ is the minimum threshold force, and d is the measured displacement of the tissue. Equation (2.7) was derived from Equation (2.7) in Section 3.1, and p is defined as the stiffness coefficient.

$$F = F_T(e^{pd} - 1) \tag{2.7}$$

The stiffness coefficient p and the modulus coefficient p can be related by the tissue thickness t_0, by the relationship shown in Equation (2.8).

$$p = \frac{q}{t_0} \tag{2.8}$$

Figure 2.16 below shows four samples plotted and a fitted curve with $p = 35$. There is good agreement between the collected data and the selected fitted curve.

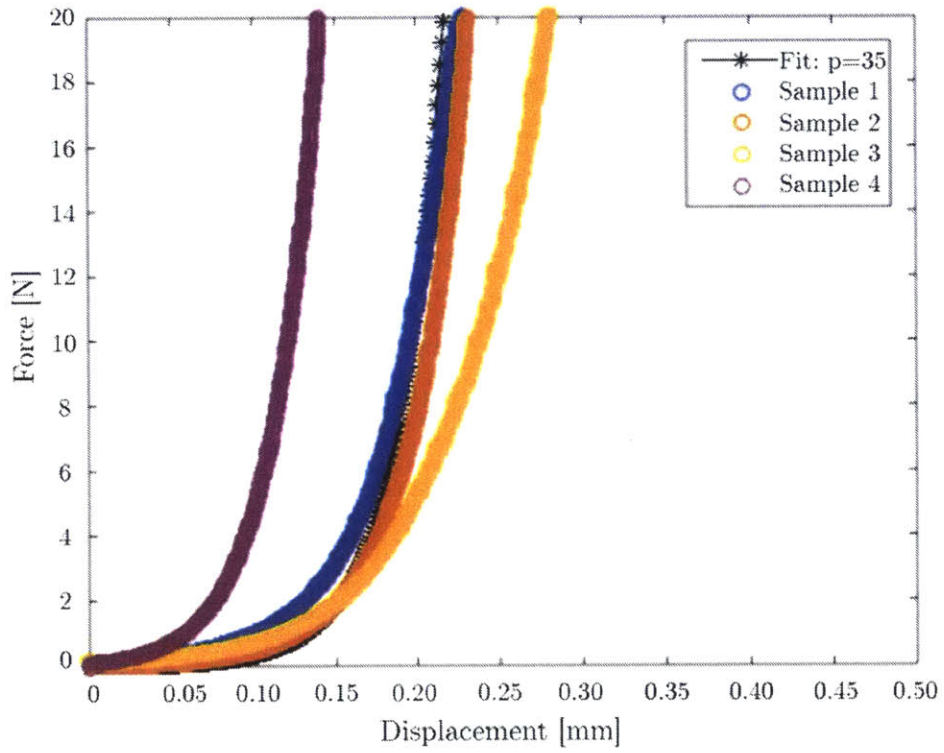

Figure 2.16: Example shear stiffness curves [28].

The material properties and calculated p and q values are shown in Table 2.3 below.

Table 2.3: Measured compression stiffness properties.

Parameter	Skin	Muscle	Units
Tissue Thickness	0.455 ± 0.063	1.030 ± 0.380	mm
q Value	11.49 ± 0.14	7.85 ± 2.50	---
p Value	25.50 ± 3.54	7.70 ± 0.42	---

The calculated modulus and thickness values from the tests performed agree with values found in literature. While there are not published data for all the tissue types measured in the test, the values measured fall within the range that was found in literature for human and bovine skin and muscle. Both the measured and literature values are presented in Table 2.4 below.

Table 2.4: Measured and literature material property values.

Type of Tissue	q Value Range	Thickness Range [mm]	Source
Mouse Skin (Cheek)	11.49 ± 0.14	0.455 ± 0.063	Measured
Mouse Muscle (Cheek)	7.85 ± 2.50	1.030 ±0.380	Measured
Mouse Skin (Hind Limb)	10.77 ± 2.03	0.278 ± 0.102	[20]
Rabbit Muscle (Soleus)	4.6 - 7.4	---	[23]

The stress-strain curve for the skin will be used as a material property in the FEA presented in Chapter 3.

2.4.2 Shear Stiffness

The shear stiffness of the tissue was calculated using Equation (2.6). This value includes the static friction between the ABS contact and the mouse skin, which is difficult to measure or quantify. The purpose of this test is to determine whether the stiffness of the contact—including both shear stiffness of the skin and the static friction involved—is significant relative to the compressive stiffness for each contact point. Therefore, a measurement of the combined quantity for the shear stiffness is sufficient.

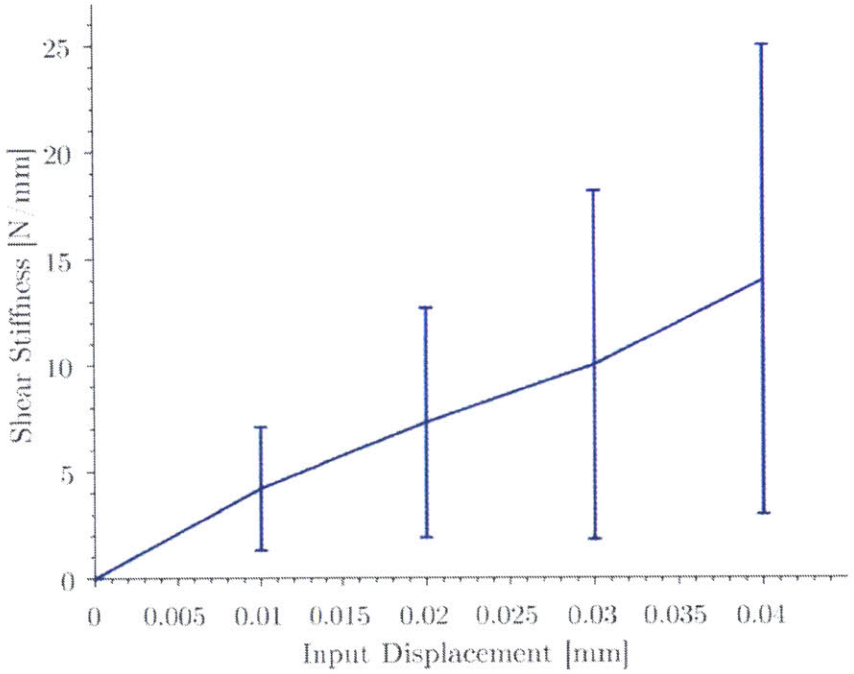

Figure 2.17: Shear stiffness as a function of input displacement.

Figure 2.17 shows the shear stiffness as a function of input displacement. As the skin is pulled taut, the stiffness increases in that direction, as expected. As seen from the error bars, the measured values vary greatly; this is likely the result of "stick/slip," where the static friction force in some trials is overcome by the applied shear force, and the skin slips against the contact, but not in others. The final values measured and calculated are summarized below in Table 2.5.

Table 2.5: Final shear stiffness values

Input Displacement (δ) [mm]	Mean Measured Displacement (δ_y) [mm]	Mean Shear Stiffness (k) [N/mm]	Shear Standard Deviation (σ_k) [N/mm]
0	0	0	0
0.01	0.0050	4.2	2.9
0.02	0.0086	7.3	5.4
0.03	0.0113	10.0	8.2
0.04	0.0130	14.0	11.0

For the first $10\mu m$ of applied shear displacement under a $5N$ contact force, the average shear stiffness was $4.27N/mm$. This stiffness is two orders of magnitude less than the compression stiffness of the skin at the same displacement ($141.0N/mm$). Therefore, the shear stiffness—including frictional force—can be neglected, and each device contact only applies constraint normal to the contact surface.

CHAPTER

3

QUASI-CONFORMAL CONTACT SYSTEM MODELING

This chapter develops the method for modeling quasi-conformal contacts in systems with compliant materials. The assumptions and equations necessary for implementing this approach are presented. The holder device is modeled as a system of springs, and each contact is modeled as an individual spring to determine an effective stiffness. The stiffnesses are then combined to determine the overall stiffness of the system.

The overall system model is presented in Section 3.1. An overview of conformal contacts and motivation for the application is discussed in Section 3.2. In Section 3.3, the methods used for nonlinear Finite Element Analysis of point and conformal contacts are presented. Finally, the model limitations are explained in Section 3.4.

3.1 System Modeling

The holding method used in this thesis can be modeled as a system of springs, where each point of contact between the holder and the mouse is an individual spring with a stiffness. A schematic of the spring system for the proposed concepts are shown in Figure 3.1 below. The two concepts below are identical other than the rear contact at the back of the mouse's head. The rear contact in the first configuration (Figure 3.1a) is effectively two point contacts, whereas the rear contact in the second configuration (Figure 3.1b) is a quasi-conformal contact approximately

matching the radii of curvature of the mouse's head. Each spring in the figure only has stiffness along the direction of the spring.

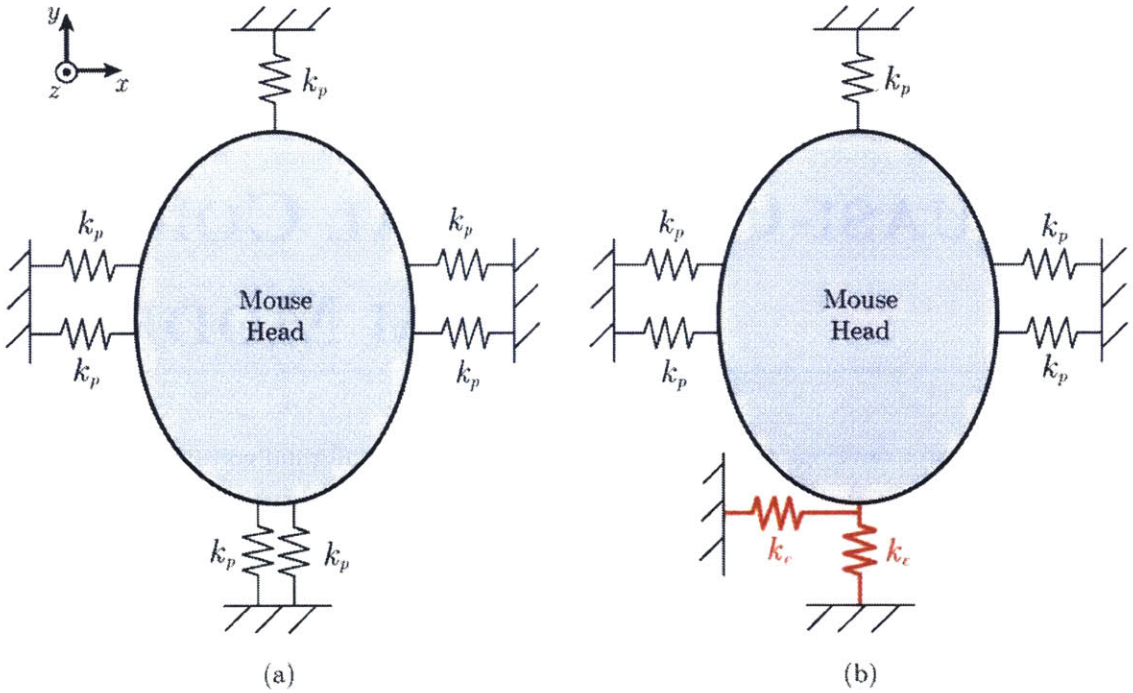

Figure 3.1: Spring systems for devices with (a) point and (b) quasi-conformal rear contacts. k_p and k_c represent effective point contact and quasi-conformal contact stiffnesses, respectively.

The conformal nature of the rear contact in configuration (b) allows the contact to apply a constraint in both the x and y directions. All springs in Figure 3.1 can also constrain in the z-axis due to the placement on the mouse head. The first configuration is the setup used in Rachel Dias Carlson's SM thesis [28]. The design of the device is discussed more in depth in Chapter 4. The stiffness of the system in the x-axis is effectively that of four springs of stiffness k_p in parallel ($4k_p$). The stiffness of the system in the y- and z-axis are $3k_p$ and $7k_p$, respectively. Section 3.3 describes an FEA method to determine the stiffnesses of both point and conformal contacts.

3.2 Conformal Contacts

Two surfaces are considered to be conformal if all points on the surface, as well as orientation angles match (see Figure 3.2). Conformal contacts are composed of two surfaces considered to be conformal relative to each other in one orientation.

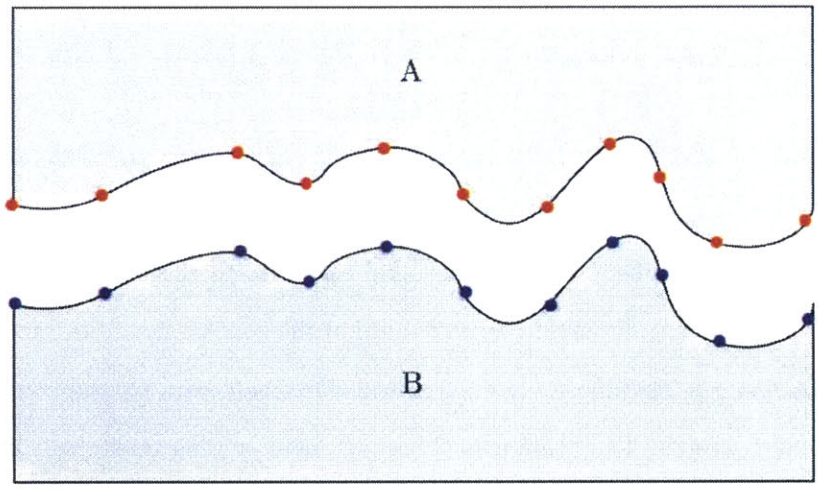

Figure 3.2: Conformal contact surfaces.

In constraint design, conformal contacts are considered to be in the realm of elastic averaging, as opposed to exact constraint due to the large surface area of constraint. As a result, conformal contacts can be designed to be significantly stiffer than a point contact, as the contact is effectively a system of springs in parallel; they can also be designed to be more robust for larger applied forces. In this particular application, a conformal contact would also allow for a greater overall contact force, as the force is distributed over a larger area. The maximum local force that skin and bone can withstand is limited, not only by material properties and yield, but also pain and injury to the animal. The trade-off for conformal contacts is the lower repeatability and possible difficulty in manufacturing a closely conformal contact.

The contact pushing on the mouse head can be modeled as many springs in series, as shown in Figure 3.3, however, the contact stiffness ($k_{contact}$) is difficult to measure individually.

The combined stiffness of the contact, skin, and muscle, however, can be modeled in FEA and also verified through experimental measurements.

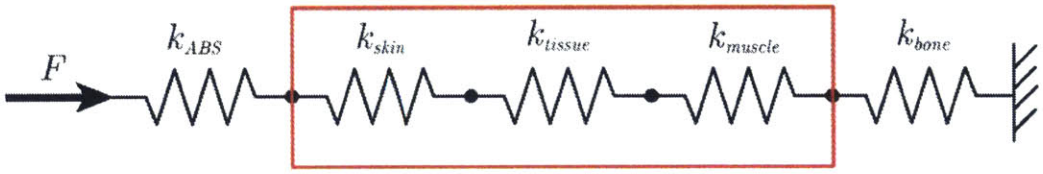

Figure 3.3: Contact joint spring system showing focus of FEA simulations.

A perfectly conformal surface is ideal, but unrealistic in real-world applications. Manufacturing errors and biological differences make perfectly conformal contacts impractical for this application. The compliance of the mouse skin can form to the shape of the rigid conformal contact, to some extent; it is important to take note of the contact distribution across the surface of the contact in this case, as uneven pressures will effectively convert the conformal contact to one or more point contacts. The "conformal" contact used in this thesis will be designed to be close to the shape of an average lab mouse, and the conformality of the designed conformal constraint to the mouse's head is investigated. This type of contact is a quasi-conformal contact, as shown in Figure 3.4 below.

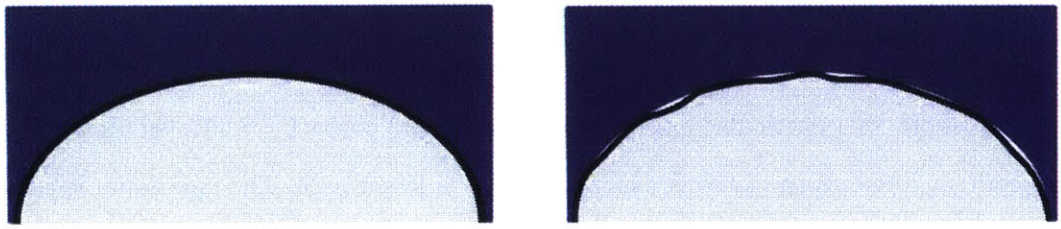

Figure 3.4: (a) Perfectly conformal contacts as compared to (b) quasi-conformal.

An anatomically correct CAD model of a lab mouse was measured to determine the appropriate radii of curvature for the conformal contact. The back of a mouse's head is

approximately the shape of an ellipsoid with two radii of curvature. Therefore, the rear constraint is designed to have two radii of curvature, shown in Figure 3.5 below.

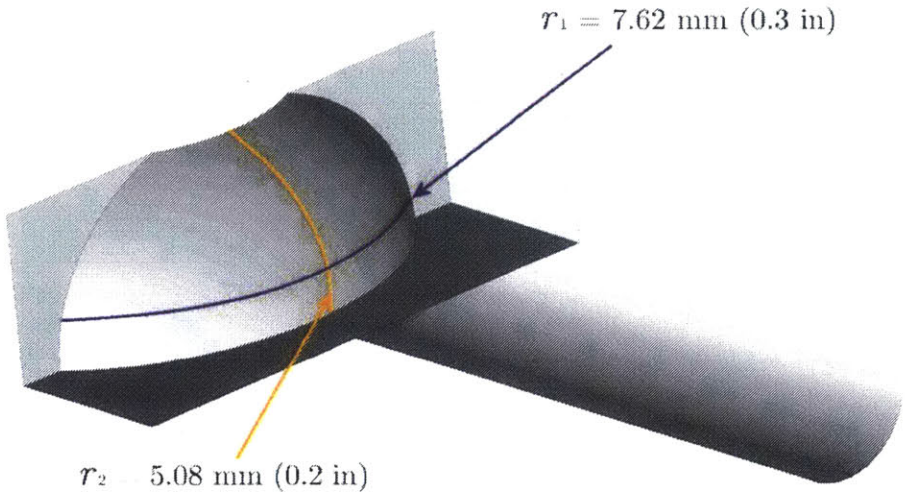

Figure 3.5: Back-of-head constraint shape with labeled arcs of curvature.

In this thesis, the conformal nature of the contact was determined by using Fujifilm Prescale Extreme Low Pressure (4LW) sensing film, and comparing that pressure gradient the contact pressure in FEA. If the two were qualitatively similar, and the contact has no points where the contact pressure is 0, then the contact can be modeled as conformal.

3.3 Finite Element Simulation of Contact Models

Finite Element Analysis was used to model the overall contact stiffness for both conformal and point contacts. The methods for simulation of point contacts and conformal contacts are described in Sections 3.3.1 and 3.3.2 respectively. Point contact modeling has been modeled before in Rachel Dias Carlson's SM thesis; however, the modeling method is different and the applied displacement ranges tested do not allow for comparison to FEA simulations performed for conformal contact modeling in Section 3.3.2. It was necessary to run similar simulations for both contact types for both validation and comparison.

3.3.1 Point Contact FEA Modeling

The SolidWorks model for the FEA simulation of a point contact is shown in Figure 3.6. A displacement is applied on a $0.79mm$ diameter circular surface on a small piece of mouse tissue of thickness $1.5mm$—average total thickness of mouse skin and muscle. The skin and muscle were combined into one piece of tissue to simplify the simulation and decrease run time significantly. An equivalent stress-strain curve of the combined materials was found and used for the material property settings in the simulation. The bottom of the tissue was fixed, while a roller/slider constraint was placed on two opposing sides to constrain the tissue. The ABS contact and mouse bone did not need to be included as parts in the model, as the stiffnesses of those parts are significantly greater than the stiffness of skin and can be considered to be rigid [28].

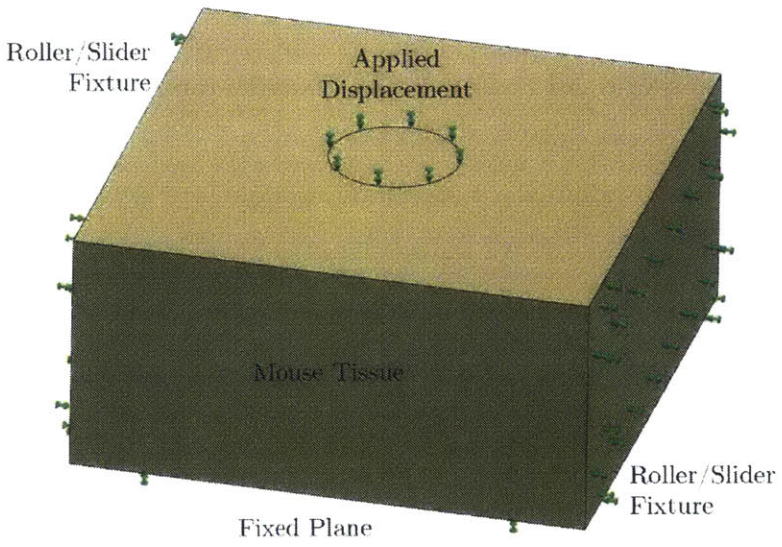

Figure 3.6: SolidWorks setup for point contact FEA simulation.

The results from the simulations are shown in Table 3.1.

Table 3.1: Point contact FEA results.

Displacement $[mm]$	Resultant Force $[N]$
0	0
0.01	4.41×10^{-5}
0.025	11.7×10^{-5}
0.05	25.9×10^{-5}
0.075	42.8×10^{-5}
0.10	63.2×10^{-5}

3.3.2 Conformal Contact FEA Modeling

For the FEA model, the conformal contact shape was simplified into an arc. The arc is representative of the contact shape and is more practical when running multiple simulations. The CAD model used in the FEA is shown in Figure 3.7. The skin and muscle were combined into a single piece of tissue, as they were for the point contact modeling. The ABS contact and bone were included in this model to geometrically constrain the tissue as it deforms. The tissue was bonded on the underside to the bone, while the interface between the tissue and contact was set to "No Penetration." The bottom of the bone was fixed and roller/slider constraints were added to the remaining necessary sides of the bone and curved contact.

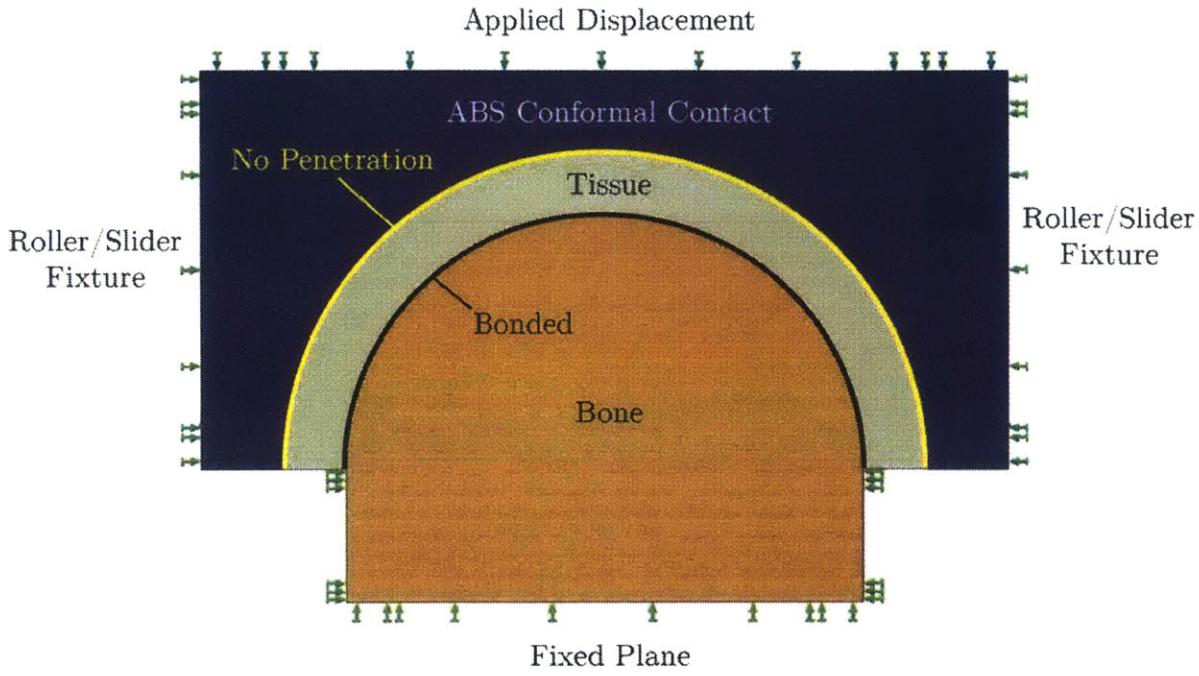

Figure 3.7: SolidWorks setup for conformal contact FEA simulation.

The results from the FEA simulations are shown below in Table 3.2.

Table 3.2: Conformal contact FEA results.

Displacement $[mm]$	Resultant Force $[N]$
0	0
0.01	0.0016
0.05	0.0089
0.10	0.0229
0.15	0.0440

In addition to the force-displacement data, the contact pressure distribution along the arc was also taken and will be compared to the pressure distribution recorded by the pressure sensing film during experimental testing.

3.3.3 FEA Results Discussion

The results from both point and conformal contact simulations are plotted in Figure 3.8. As expected, the stiffness of the conformal contact joint is higher than that of a point contact.

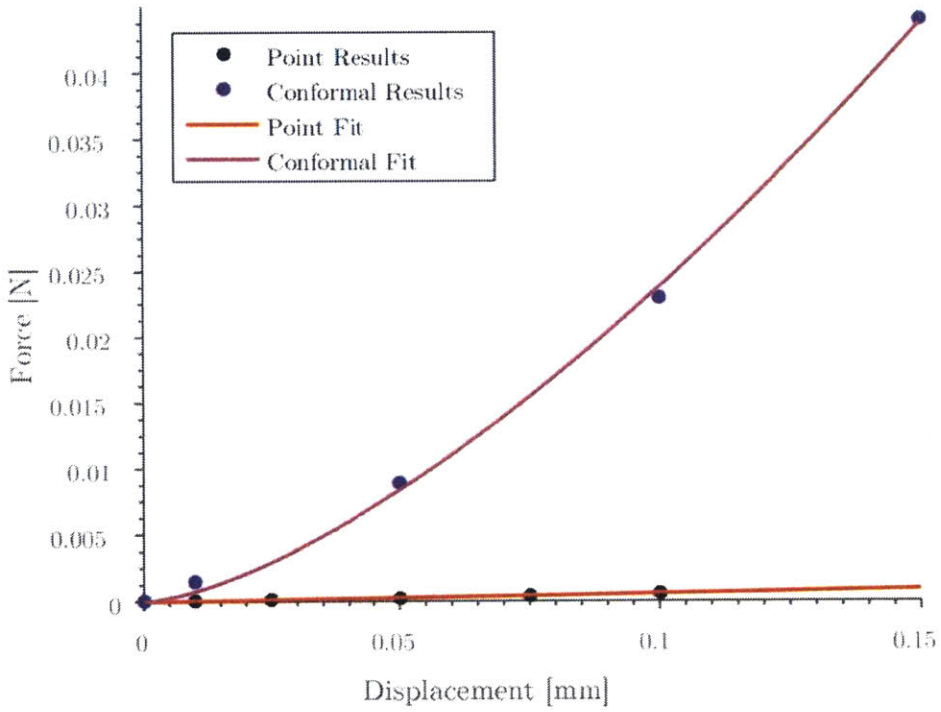

Figure 3.8: Force-displacement curves for point and conformal contacts from FEA.

Linearizing the stiffness about a $0.1mm$ displacement, the stiffnesses for both point and conformal contacts can be found—$0.068N/mm$ and $0.358N/mm$ respectively—and combined with the spring system model presented in Section 3.1. The overall stiffnesses in all 3 axes for both configurations shown in Figure 3.1 are shown below in Table 3.3.

Table 3.3: Point vs. conformal stiffness comparison (FEA).

Axis	Point System Stiffness (k_p) $[N/mm]$	Conformal System Stiffness (k_c) $[N/mm]$	Ratio (k_c/k_p)
x	27.1	385.0	14.2
y	20.3	364.7	17.9
z	47.2	391.8	8.3

The contact pressure along the arc is plotted in Figure 3.9a below; these results will be compared to the contact pressure empirically measured by the pressure sensing film during testing of the device. The contact pressure varies as expected along the arc. The angle alpha (α) is defined as shown in Figure 3.9b.

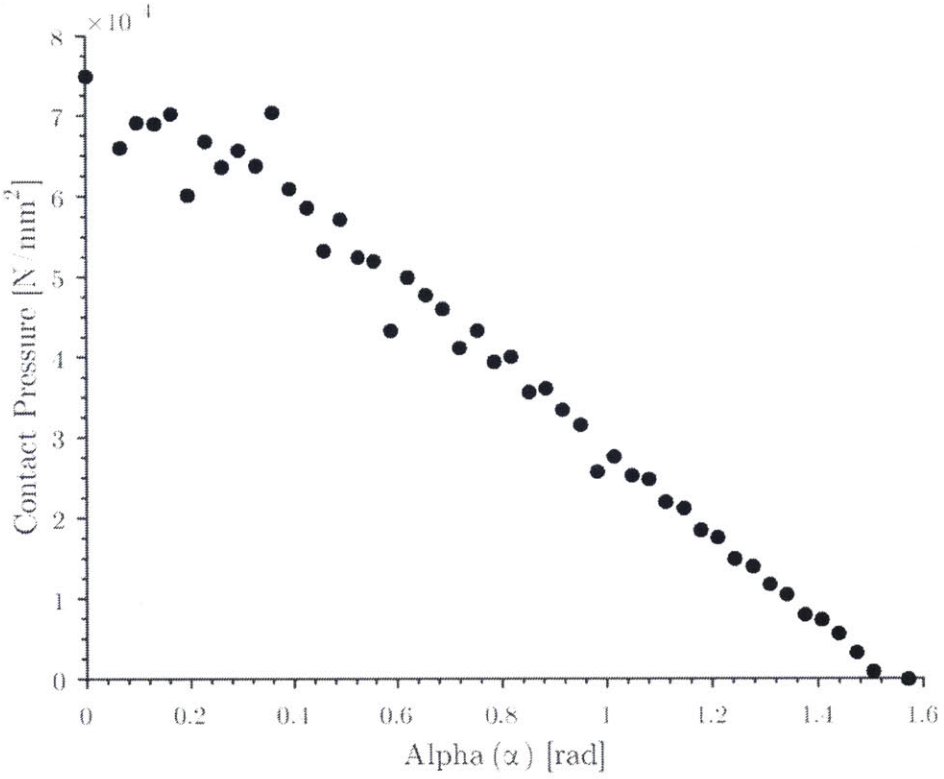

(a)

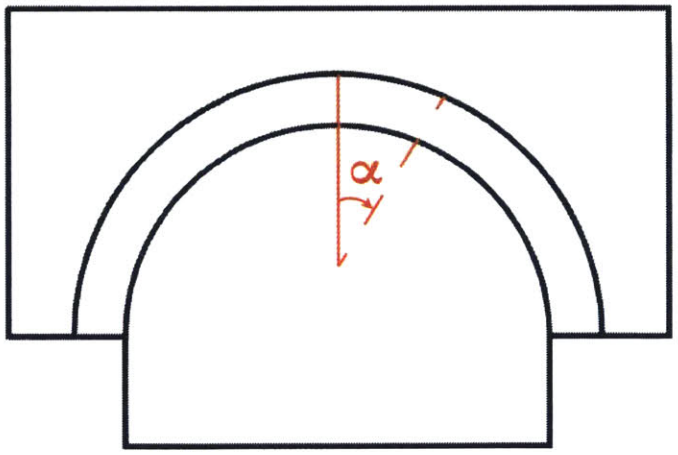

(b)

Figure 3.9: (a) Resulting contact pressure along arc of conformal contact and (b) the definition of angle alpha (α).

3.4 Limitations

The spring system portion of this model assumes in the current setup that the stiffness of the point contact constraint is the same for all of the interfaces between the device and the mouse head. Given further material property measurements of skin at different locations around the mouse's head, the model could be further refined to account for these differences. The model in its current configuration does not account for moment stiffness of any of the constraints. A future version of the model could be built to include the moment stiffnesses of the constraints, which would improve the theoretical performance of the device even further. The model currently would produce a worst-case estimate of the device performance.

The FEA for this model has only been able to solve for small applied displacements; these displacements are much smaller than the displacements applied in experimentation. The stiffnesses determined for the overall contact stiffness will not be accurate if they are extrapolated. The relative stiffnesses between the point and conformal contacts may also be different at higher displacements.

CHAPTER

4

PROTOTYPE DEVICE DESIGN

This chapter presents the design of the prototype device. Functional requirements of the device are presented in Section 4.1. The mechanical design of the device is discussed in Section 4.2 along with other design considerations, such as modularity and ability to incorporate instrumentation.

4.1 Functional Requirements

The functional requirements for the prototype device are presented in Table 4.1:

Table 4.1: Functional requirements for prototype device.

Property	Required	Units
Instantaneous Movement (lateral)	<1	μm
Instantaneous Movement (axial)	<0.7	μm
Overall size	50×50	mm

The *instantaneous movements* refer to short timescale movements such as breaths and heartbeats. The lateral and axial directions are relative to the objective lens. The *overall size* of the device needs to remain within a $50mm$ square to fit underneath most microscope setups comfortably.

4.2 Mechanical Design

The prototype consists of a structure with modular and adjustable contact points for easy testing. The SolidWorks model of the complete prototype device is shown in Figure 4.1.

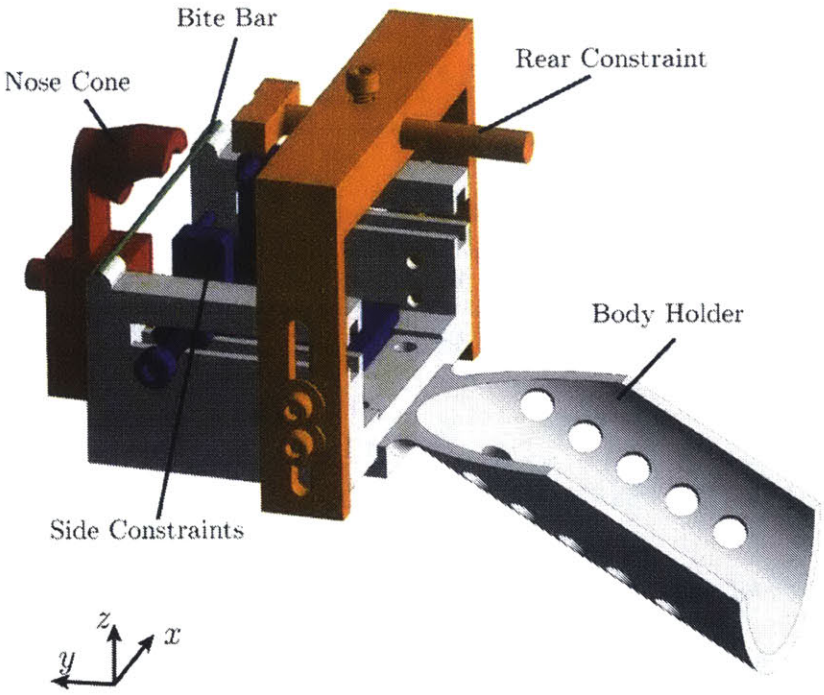

Figure 4.1: CAD model of prototype restraint device.

The purpose of this version of the device was to test the effectiveness of quasi-conformal contacts. Therefore, modularity of the contacts, rather than user interface, was the main focus of the design. All of the contact points except for the rear contact are designed to be point contacts. The rear contact is the only quasi-conformal interchangeable contact, so that the effect of the quasi-conformal contact can be isolated.

4.2.1 Constraint Locations

The constraint locations for this device were chosen based on kinematic constraint theory, mouse skull geometry, and expert biologist suggestions. To fully constrain any rigid body, exactly six points are necessary. In practice, however, it was necessary to have more than 6 contacts to fully constrain the mouse head. The locations of the constraints are shown on a mouse head in Figure 4.2. The colors of the arrows correspond to the components of the same color in Figure 4.1.

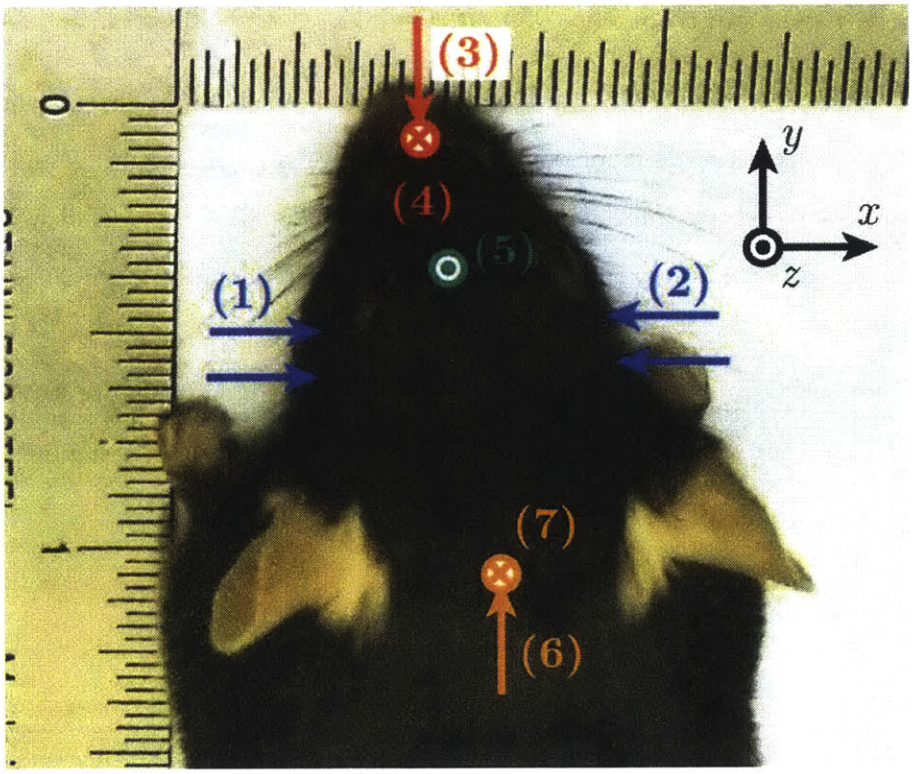

Figure 4.2: Constraint locations on mouse head.

The six degrees of freedom of the mouse head are shown in Table 4.2. The constraints (1) and (2) represent two point contacts each. This design decision was made ultimately for the increased comfort of the mouse. These two point contacts are also strategically located on the skull to effectively constrain in the z-axis. This system is ultimately over constrained, but the elastic averaging is necessary due to the low stiffness of the mouse tissue.

Table 4.2: Degrees of freedom of motion and corresponding constraints.

Degrees of Freedom	Constraints
x	(1) & (2)
y	(3) & (6)
z	(1), (2), (5), (4) & (7)
θ_x	(5), (4) & (7)
θ_y	(1) & (2)
θ_z	(1) & (2), (3) & (6)

4.2.2 Holder Structure

The structure of the holder was designed to be fully modular, so that it would be able to accommodate various sizes of laboratory mice. For ease of manufacturing and to allow for customization, the structures interfacing with the mouse were 3D printed from ABS. The holder was then connected to an adjustable-height Thorlabs vertical mount and attached to an optical table during testing.

The two constraints on either side of the mouse head are on flexible structures that press against the mouse head when the bolts are tightened. This mechanism is highlighted in Figure 4.3.

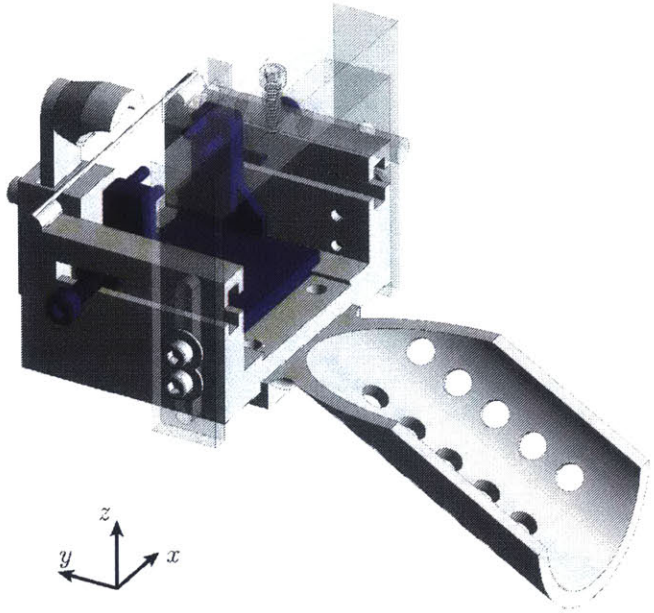

Figure 4.3: CAD model of prototype device. Side constraints shown in blue.

The nose cone—highlighted in red in Figure 4.4—is also fully adjustable in both the y- and z-axes. The piece slides inside a slot and is secured using setscrews. The nose cone is able to restrict the translation of the mouse in both y- and z-axes, while also providing a holder for the anesthesia tube for the mouse.

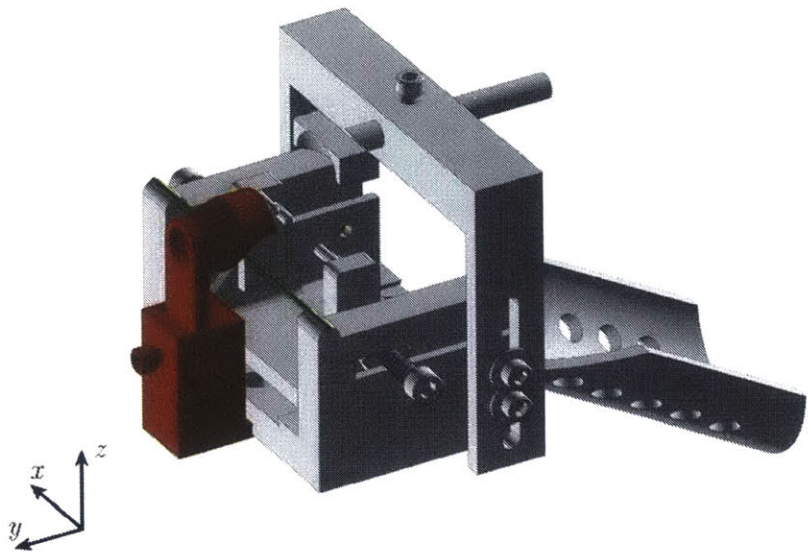

Figure 4.4: CAD model of prototype device. Nose cone shown in red, and bite bar shown in green.

The bite bar—shown in green in Figure 4.4—is used for initial positioning of the mouse prior to applying preload on each of the designed constraints. It also pairs with the nose cone and rear contact to apply an upward normal force on the mouse to constrain in the z-axis.

4.2.3 Rear Contact Probes

The rear contact is adjustable in both the y- and z-axes and is placed on the mouse after all other constraints are put in place. This contact is attached to structures that also allow for y- and z-axis adjustments. The angle of application (θ_y) can also be adjusted for positioning relative to the mouse.

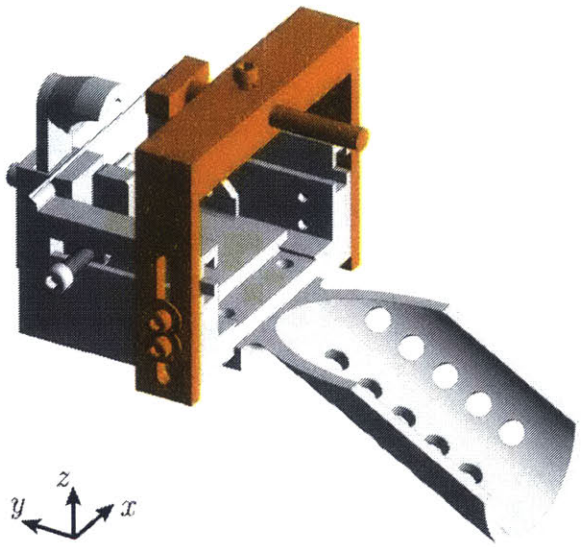

Figure 4.5: CAD model of prototype device. Rear contact structures shown in orange.

This contact was also designed so that the force applied by the rear contact could be easily measured with a force sensor. The post behind the contact protrudes behind the structure, as seen in Figure 4.5, and force is applied from the back. The position of the contact is secured by the bolt acting as a set screw.

Two sizes of quasi-conformal contacts were used. These contacts have identical radii of curvature, but have different surface areas. A comparison of the two contacts is shown below in Figure 4.6.

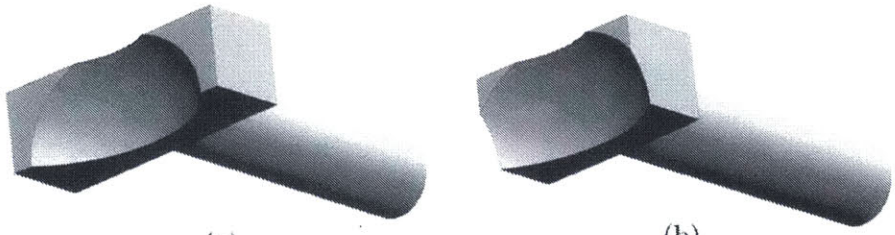

(a) (b)

Figure 4.6: (a) Long and (b) short quasi-conformal contacts.

4.2.4 Instrumentation Integration

A separate structure designed to hold capacitance probes in adjustable locations was designed, so that mouse displacement measurements could be made on this device. This structure was designed so that three capacitance probes measuring displacement in all three directions could be used. This structure, shown below in Figure 4.7, was machined from aluminum with set screws to hold the probes in place. The structure was then attached to an adjustable Thorlabs vertical holder for fixturing on an optical table.

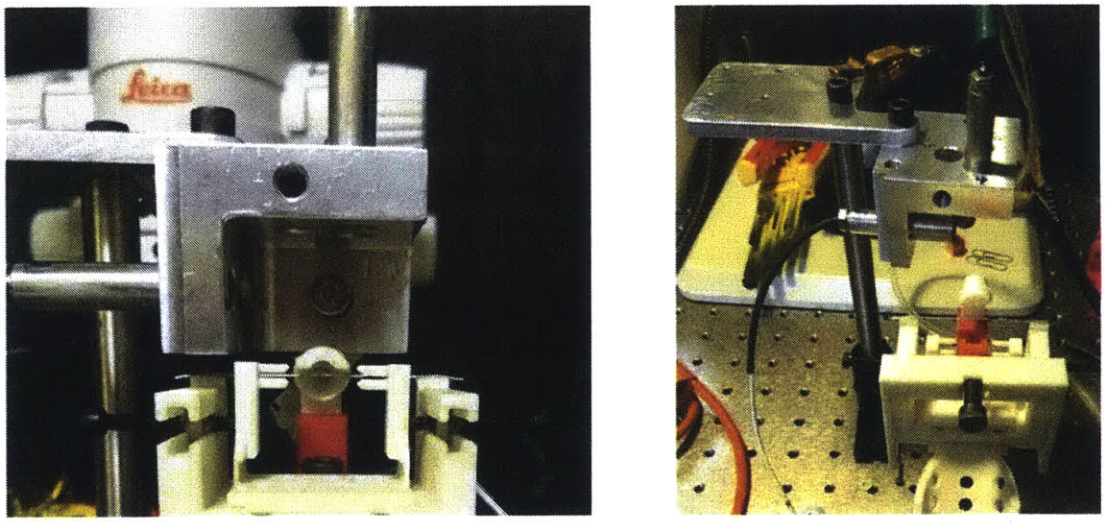

(a) (b)

Figure 4.7: (a) Back and (b) overall view of capacitance probe holder.

CHAPTER

5

EXPERIMENTAL DESIGN & PRELIMINARY TESTING

The experimental design, preliminary testing, and resulting performance of the prototype device is described in this section. Section 5.1 outlines the experimental setup and preparation procedure. Section 5.2 details the data collection procedures and special measures taken during testing to collect the data required. Results are discussed in Section 5.3. Section 5.4 details the additional modeling that was necessary for this device.

5.1 Experimental Setup

The purpose of this preliminary testing is to validate the performance of the device against the model. A mouse was anesthetized and placed in the prototype device; the movement of the mouse in 3 axes was then measured and recorded over time under various conformal constraint conditions. The protocol for this testing procedure has been officially approved under the protocol number 2015N000231. All testing on mice was performed at the MGH Center for Systems Biology.

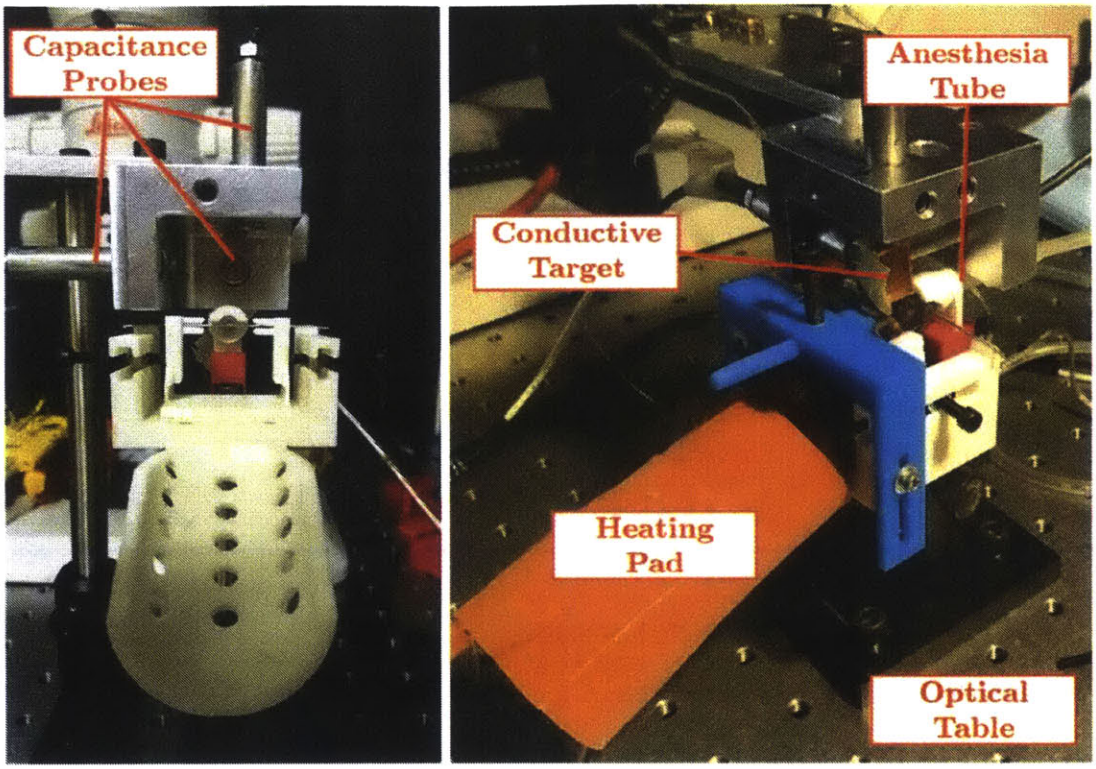

Figure 5.1: (a) Back view of the holder and capacitance probe setup. (b) Final testing setup for data collection.

5.1.1 Mouse Preparation Procedure

Capacitance probes were used to accurately, and with high precision, measure the movement of the mouse head. Capacitance probes require a conductive measuring target; therefore a plastic block with a copper conductive surface was attached rigidly to the mouse's skull using the following protocol:

1. Anesthetize the mouse. The mouse strain used for this testing was C57BL/6.
2. Place the mouse in the prototype restraint device without the back support. Make sure the anesthesia tube is placed properly in the nose cone. This makes it easier to make sure the block is glued in the proper orientation so that the sides are as normal as possible to the measurement axes. The back support is left off in order to allow easier surgical access for the scientist.

3. Remove hair from top and back of the head. This allows for visible confirmation that the constraints are properly contacting the head.
4. Remove skin from the top of the head, exposing the skull.
5. Fix the conductive block/measuring target to the top of the skull with super glue.
6. Allow 5-10 minutes for the super glue to fully dry. Touch up super glue as needed. The specimen is now prepared for the testing procedure.

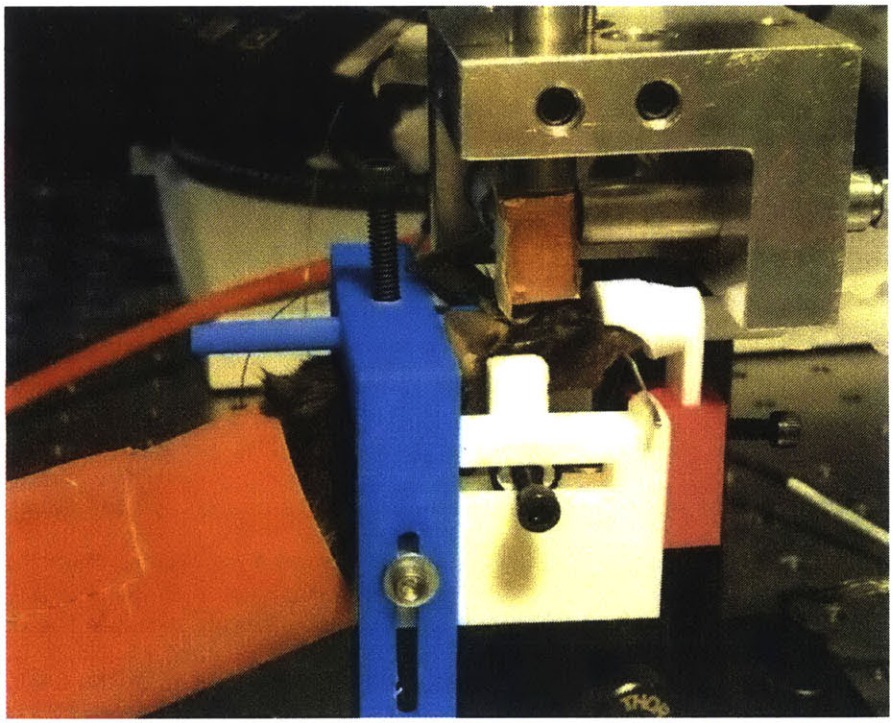

Figure 5.2: Mouse in holder with measuring target attached.

5.1.2 Instrumentation Setup

The capacitance probes used in this experiment were the Lion Precision non-contact capacitance gauges used with the DMT12 dual sensitivity probe driver modules. The capacitance probes were mounted on a fully adjustable holder. The capacitance probe holder as well as the device were bolted rigidly to an optical table to minimize the effects of exterior movements. The capacitance probes record data at a rate of $1000Hz$.

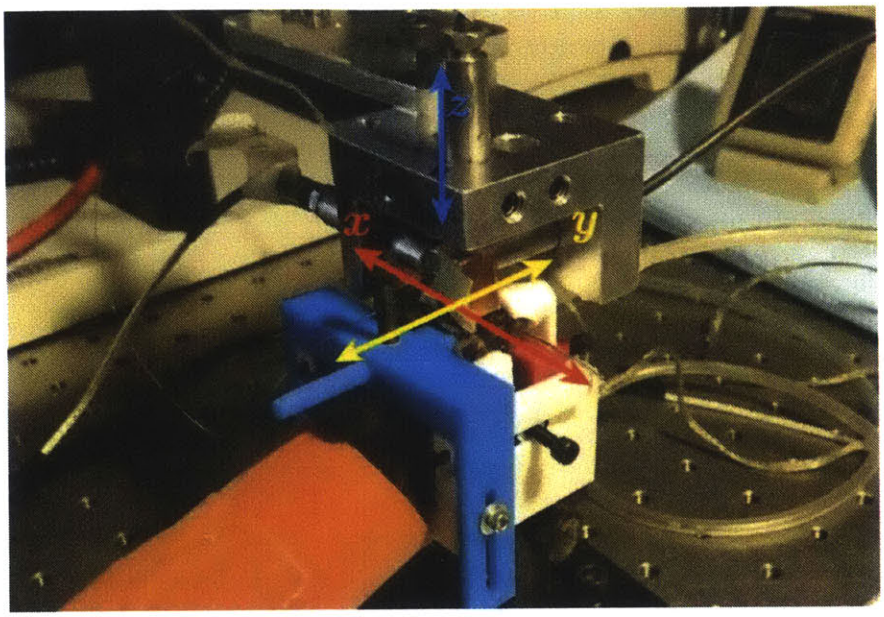

Figure 5.3: Capacitance probe positioning with labeled axes.

The three capacitance probes as well as a force pad sensor were set up with a National Instruments data acquisition board and myRIO. A LabVIEW program was set up to record continuous data for all four sensors over indefinite time on command. All the data would be saved in a spreadsheet file and was then post-processed to achieve final results. The Fujifilm Prescale Extreme Low Pressure (4LW) sensing film was used to qualitatively measure the contact pressure distribution between the quasi-conformal contact surface and the back of the head. The resulting pressure distribution from the film is shown below in Figure 5.4. While the surface area was so small that taking quantitative measurements was not practical, the qualitative results suggest that the pressure distribution is similar to the expected relationship in Figure 3.9.

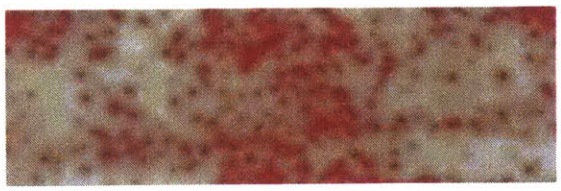

Figure 5.4: Pressure film result.

5.2 Device Performance Testing

To determine the effectiveness of the back conformal support, two separate conformal support sizes were tested and measured at two application forces. Data was also recorded for trials without the back support for a baseline measurement, as scientists currently image using a design with no back support.

The procedure for data collection is as follows:

1. Do any readjustments of the mouse in the restraint device and confirm the locations of each constraint.
2. Place a strip of the pressure film between the large contact and back of skull. Press the contact against the back of the head with as much force as possible without causing damage to the mouse or the skull. This part was performed by a trained scientist.
3. Hold conformal rear contact in place for 30 seconds and remove the strip. Place the colored part of the strip to the side for 30-45 minutes before imaging and comparing color shades.
4. Remove the rear contact, so a performance measurement of the current measurement device (no rear contact) can be recorded.
5. Set up the capacitive probe holder so that each probe is within $125\mu m$ of the measuring target on the skull. In all tests, all three axes were lined up and recorded simultaneously.
6. Record displacement readings for about 60 seconds.
7. Prepare to position the rear contact. Place a force sensor between the rod of the rear contact and a rigid block. Begin recording data on the force sensor and push the rear contact lightly against the back of the mouse's head, making sure that it is making full contact. Stop the data recording.

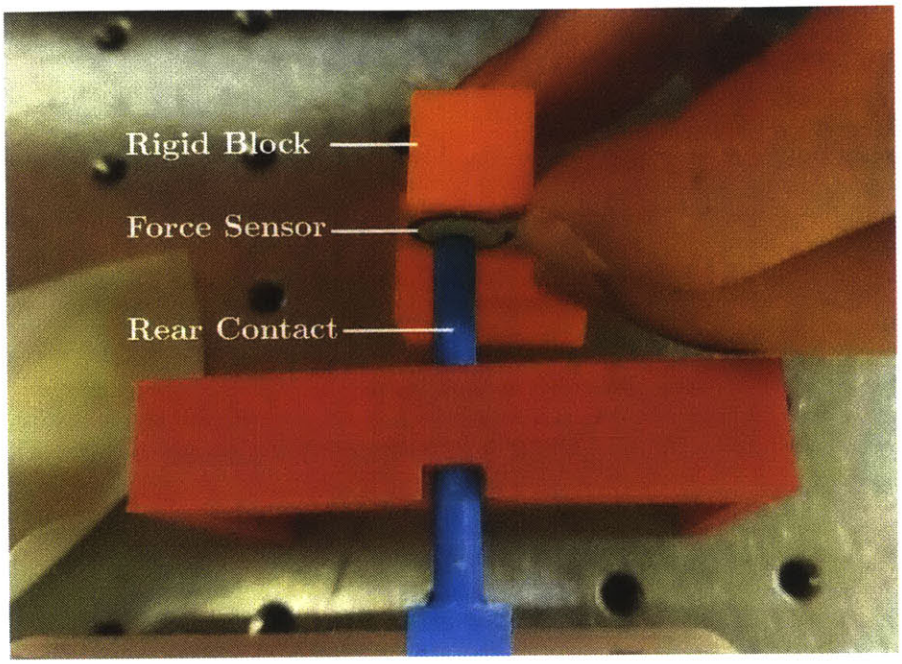

Figure 5.5: Setup to measure applied force of rear contact.

8. Repeat steps 5 and 6
9. Repeat step 7, increasing the force to the maximum force possible without causing damage to the mouse and repeat steps 5 and 6.
10. Repeat steps 7-9 for the smaller rear contact.

5.3 Results and Discussion

The noise from the capacitance probe data was smoothed using a moving average filter in MATLAB. After the filter, the displacements due to heartbeat and respiration are clearly visible in each axis, as seen in Figure 5.6.

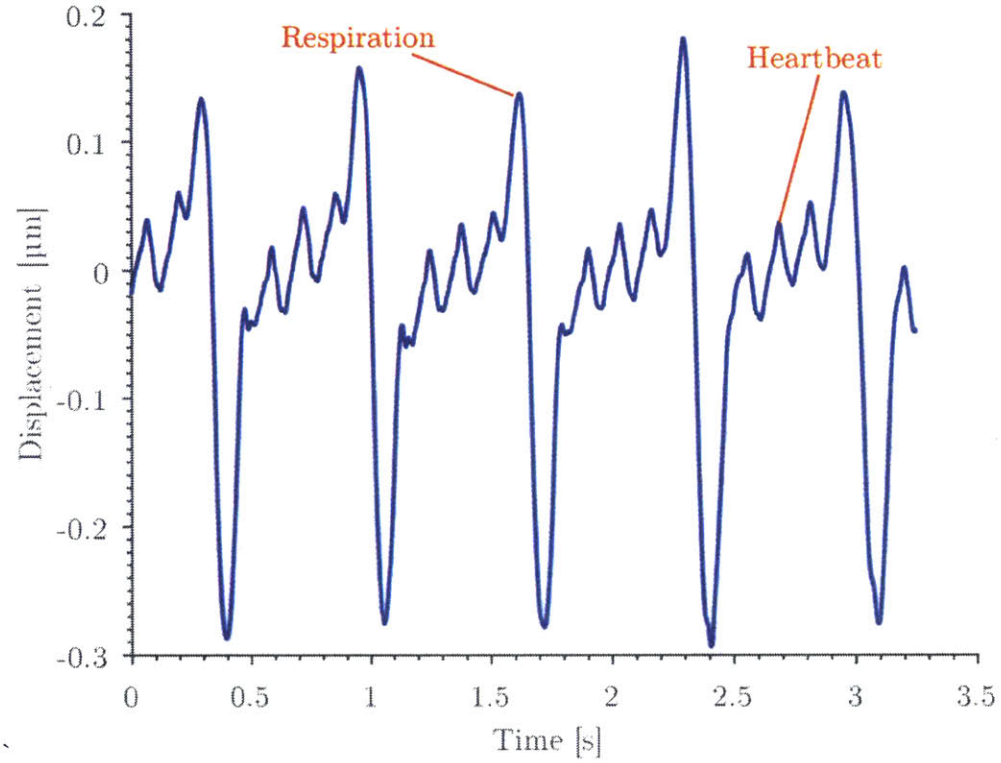

Figure 5.6: Close-up view of y-axis displacement with labeled heartbeats and respiratory movement.

To find the resultant displacement due to respiration, a series of consecutive breaths were selected from a data set, and the localized linear slow drift was subtracted from the displacement values. The consecutive breaths chosen were during the middle of the data collection session to minimize the effect of any disturbances caused by pressing the start and stop keys on the instrumentation. The height of the peaks were then measured and averaged. For heartbeats, one distinctive heartbeat peak between each pair of breaths was measured and averaged. Two conformal contacts were tested. One was a longer contact that stretched almost the full width of the back of the head, the other was a smaller one that was half the total length. Two forces were tested for each of the back contacts. The displacement values for each axis and constraint configuration can be found in Table 5.1. The uncertainty for these values was determined by adjusting the standard deviation of the averages using a t-factor.

Table 5.1: Displacement measurements for conformal constraint.

Constraint Configuration	Heartbeat Displacement [μm]			Heartbeat Uncertainty [μm]			Respiration Displacement [μm]			Respiration Uncertainty [μm]		
	x	y	z	x	y	z	x	y	z	x	y	z
Short ($3.3N$)	0.02	0.07	0.05	0.01	0.03	0.01	0.20	0.97	0.46	0.04	0.17	0.07
Long ($5.5N$)	0.01	0.06	0.02	0.01	0.02	0.01	0.06	0.63	0.23	0.02	0.15	0.04
Long ($9.1N$)	0.01	0.06	0.01	0.01	0.02	0.01	0.04	0.43	0.14	0.03	0.06	0.04
No Back	0.03	0.17	0.06	0.01	0.04	0.01	0.75	2.22	1.00	0.51	0.33	0.16

From the results shown in Table 5.1, the x-axis displacement measurements for respiration are the same order of magnitude of the noise from the capacitance probes, $40nm$. Therefore, the data collected in the x-axis direction are considered to be inconclusive. The movement of the mouse from heartbeats is also on the order of the noise of the sensors. For the remaining discussion, only the y- and z- axes will be considered, and only the measurements of the respiration—the largest cause of movement in the mouse—will be discussed. From Table 5.1, it can be noted that the setup with the larger quasi-conformal contact and higher force produced the best results. Figure 5.7 compares the z-axis displacement of the large and small quasi-conformal contacts (a) as well as the two different forces for the large conformal contact (b).

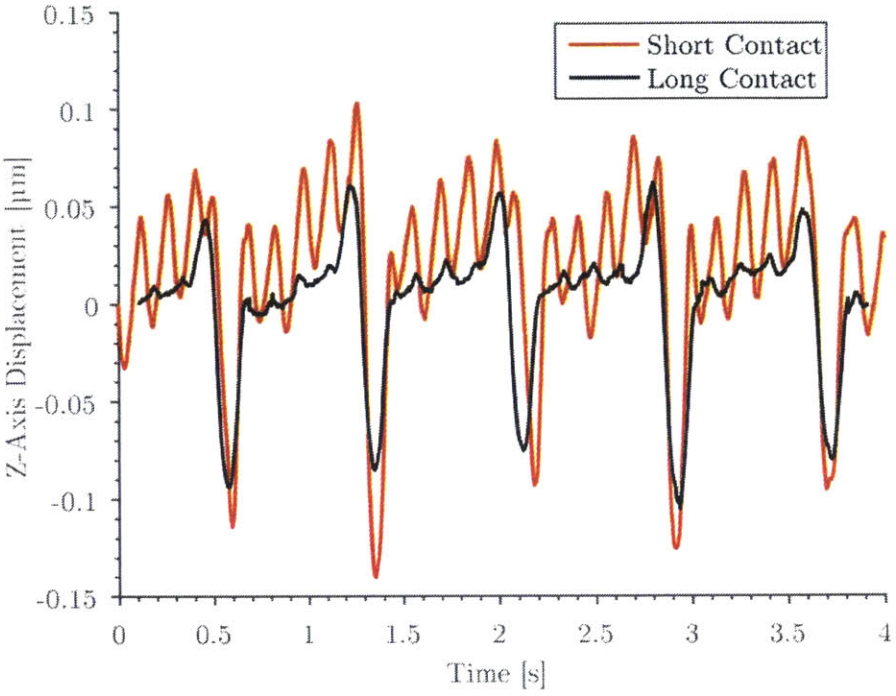

(a)

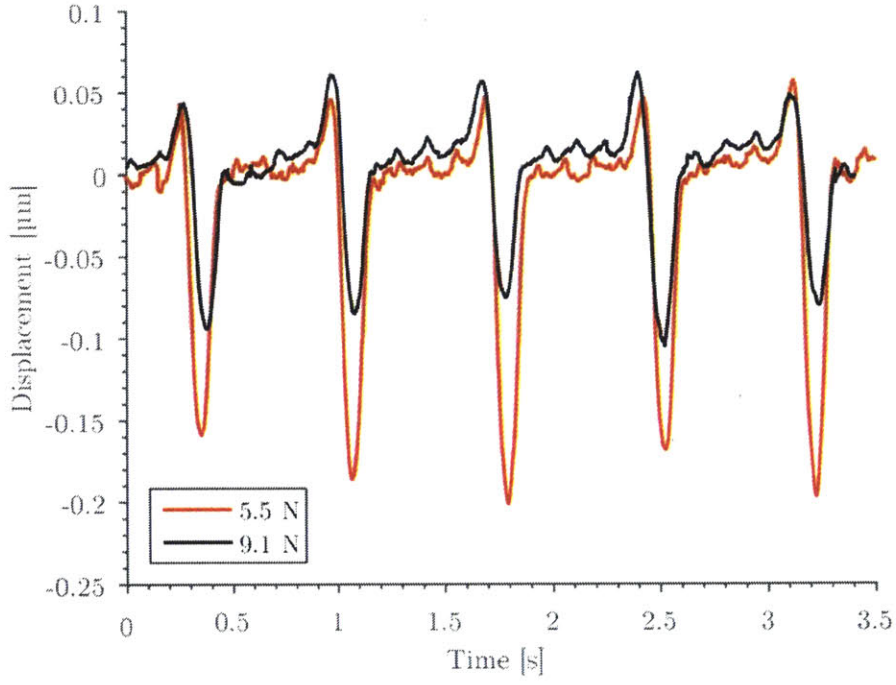

(b)

Figure 5.7: Z-axis displacement of (a) different quasi-conformal contact sizes at large force and (b) different forces applied for the large contact size.

As expected, the performance of the rear contact with the larger surface area resulted in smaller displacements, as did the higher applied force.

5.3.1 Comparison to Other Contacts

Figure 5.8 below compares the displacement data from a couple different configurations of the device. The large quasi-conformal rear contact is the best performing configuration with the least displacement in both respiration and heartbeat.

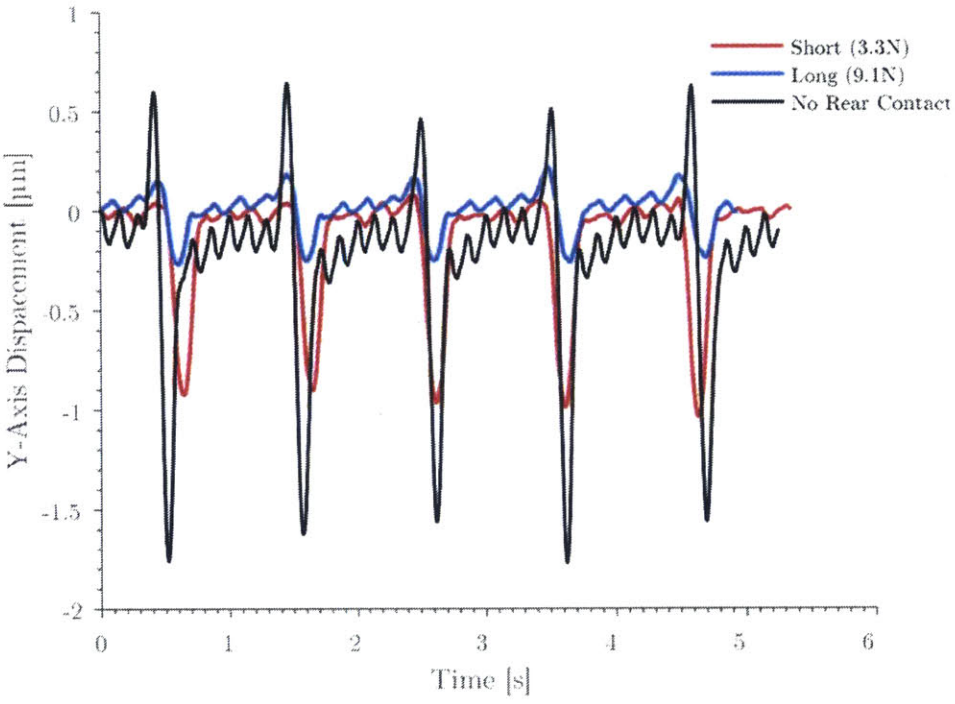

(a)

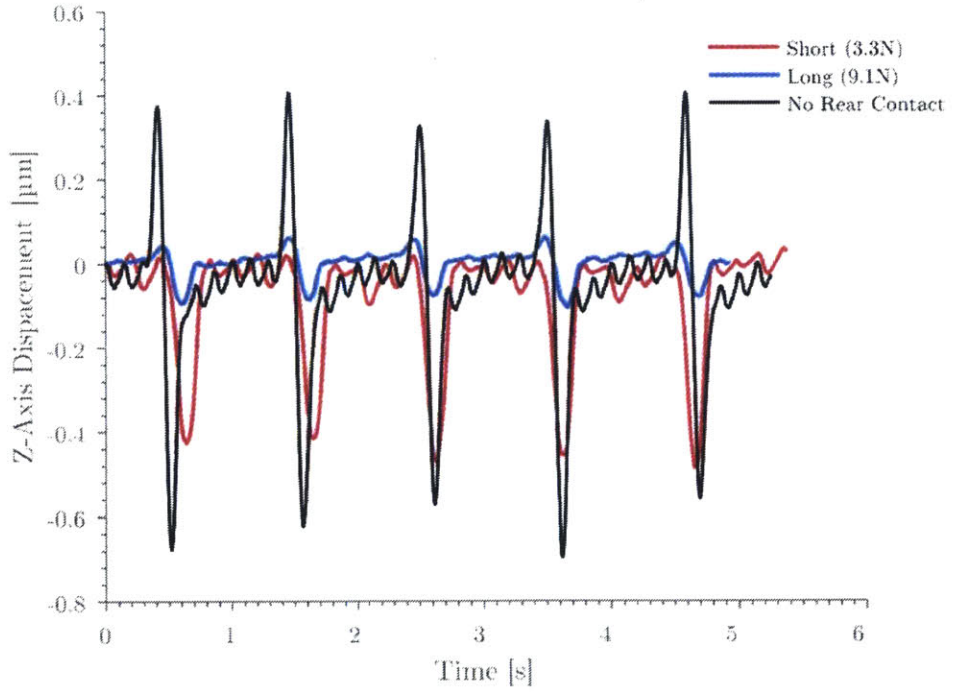

(b)

Figure 5.8: Plot comparing multiple device configurations in the (a) y-axis and (b) z-axis.

Table 5.2 below compares the displacement data from y- and z- axes for the various constraint configurations tested. Both the respiration and heartbeat movements for the restraint device with the back support are lower than any of the other strategies.

Table 5.2: Displacement data for various constraint configurations.

	Respiration Displacement [μm]	
Constraint Configuration	y	z
Short Conformal Contact (3.3N)	0.97	0.46
Long Conformal Contact (5.5N)	0.63	0.23
Long Conformal Contact (9.1N)	0.43	0.14
Point Contact	0.60	0.22
No Back	2.22	1.00

5.3.2 Comparison to Theoretical Model

To compare the measured data to the theoretical model, an effective device stiffness in each axis was calculated for the point and quasi-conformal configurations. The applied displacement of the theoretical model and the experimental data are not the same, so the stiffness values cannot be directly compared. However, the stiffness ratio between conformal and point contact configurations for the theoretical model and experimental data can be compared. The theoretical system stiffness ratio was found by dividing the conformal system stiffness (k_c) by the point system stiffness (k_p).

The experimental stiffness ratio can be calculated using Equation (5.1). The stiffness of the contact is found by local linearization of the force-displacement curve. The change in force for both the quasi-conformal and point contacts are equivalent, assuming the force exerted by the mouse for each heartbeat and each breath is relatively consistent.

$$\frac{k_c}{k_p} = \frac{\frac{dF_c}{d\delta_c}}{\frac{dF_p}{d\delta_p}} = \frac{d\delta_p}{d\delta_c} \tag{5.1}$$

where dF_i is the localized delta force on the system for the measured corresponding displacement, $d\delta_i$. The calculated stiffness ratios are presented in Table 5.3 below.

Table 5.3: Stiffness comparison for theoretical (FEA) and experimental values.

Axis	Theoretical Point System Stiffness (k_p) [N/mm]	Theoretical Conformal System Stiffness (k_c) [N/mm]	Theoretical Stiffness Ratio (k_c/k_p)	Experimental Stiffness Ratio (k_c/k_p)
x	0.027	0.385	14.2	---
y	0.034	0.365	10.8	1.4
z	0.047	0.392	8.3	1.5

The calculated theoretical stiffness ratios are about an order of magnitude larger than the experimental stiffness ratios, indicating that the theoretical model presented in Chapter 3 is not sufficient to describe the realistic system. Further modeling was then completed to explain the discrepancy.

5.4 Further Modeling

The initial model presented in Section 3.3 assumes that the tissue has not reached full compression, and the stiffness of the material nonlinearly varies with the force applied. Upon further investigation, it was hypothesized that the forces applied by the contacts have nearly fully compressed the tissue. In this case, the advantage of the conformal contact would be lessened, as the stiffness calculation becomes more like a Hertzian contact problem. However, a groove closely matching the back of the mouse head—a quasi-conformal contact—should still have a higher stiffness than an effective point contact.

A similar spring model as described in Section 3.1 was used. However, upon closer inspection of the rear contact in the point configuration, the contact interfaces with the mouse's

head in four places, because the radius of curvature is smaller than that of the head (see Figure 5.9).

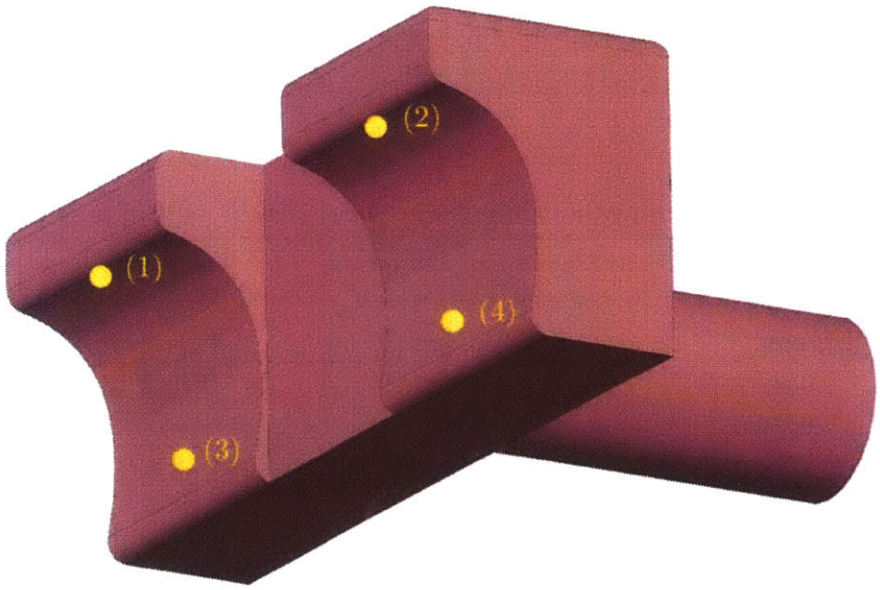

Figure 5.9: Rear contact geometry for point contact configuration.

All four points constrain the head in the y-axis, but only (1) and (2) constrain in the z-axis. The new spring model for the point contact configuration is shown in Figure 5.10. The stiffness of all springs in the figure is k_p; the two springs in red only act in the y-axis, but not the z-axis. The quasi-conformal contact configuration spring model remains the same.

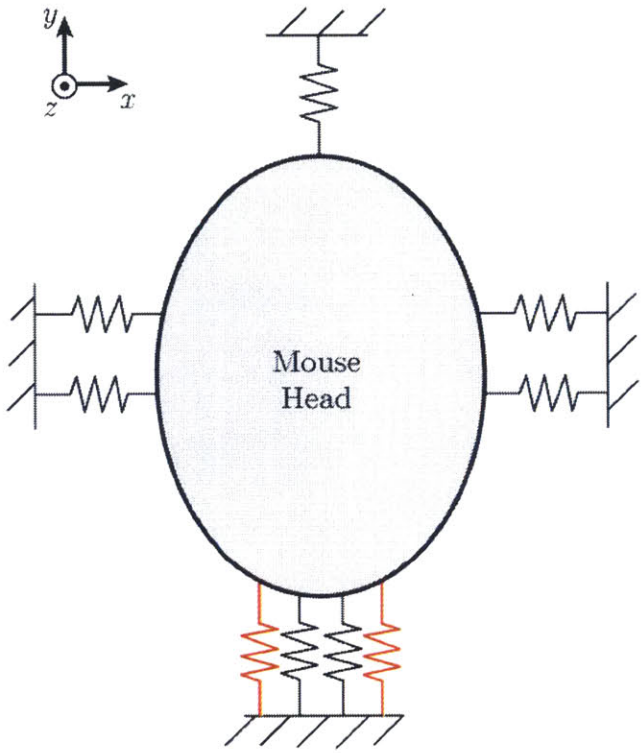

Figure 5.10: Updated system spring model for point contact configuration.

The stiffnesses of the point and quasi-conformal contact springs were found using Hertzian Contact Theory presented in Layton Hale's PhD Thesis [32]. The equations used are presented in Appendix C. Figure 5.11 shows two sets of three-dimensional bodies, each with two radii of curvature, in contact. In Figure 5.11a, both bodies are concave with positive radii of curvature; the lower body in Figure 5.11b is convex with two negative radii of curvature. This essentially describes an ellipsoid in contact with an ellipsoidal groove, and will be the model used for the work in this thesis.

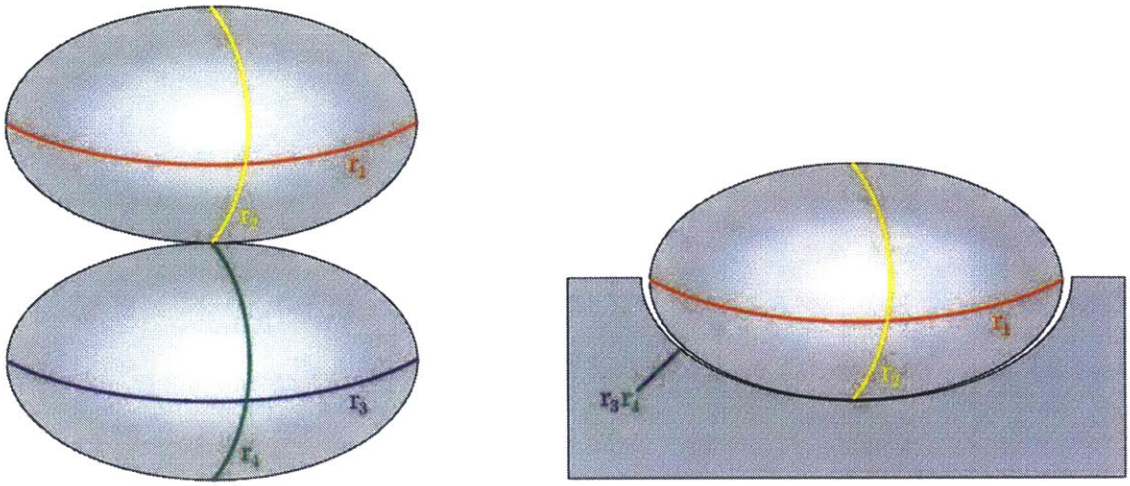

(a) (b)

Figure 5.11: Diagram with (a) two convex ellipsoids and (b) one concave, one convex ellipsoid.

The values for the input variables to the Hertzian contact calculations are shown in Table 5.4. The elastic modulus and Poisson's ratio for mouse bone and ABS were used for the ball and grooves, respectively.

Table 5.4: Inputs to Hertzian contact calculations.

Variable	Symbol	Value	Units
Mouse Head (Ball) Major Radius	r_1	0.00762	m
Mouse Head (Ball) Minor Radius	r_2	0.00508	m
Major Radius Correction Factor (Point)	β_{point_1}	-10000	---
Minor Radius Correction Factor (Point)	β_{point_2}	-10000	---
Major Radius Correction Factor (Conformal)	$\beta_{conformal_1}$	-1.01	---
Minor Radius Correction Factor (Conformal)	$\beta_{conformal_2}$	-1.01	---

The head was modeled as a "ball" with radii of curvature $7.62mm$ and $5.08mm$, as measured from a CAD model for both configurations. In the point contact configuration, the rear contact was modeled as a groove with an effectively infinite radius of curvature, because the portions of the rear contact that interface with the mouse head are flat. In the conformal contact

configuration, the rear contact was modeled as a groove with slightly larger radii of curvature. The differences in radii of curvature between the "ball" and "groove" are described by β_1 and β_2, as shown in Equation (5.2). The closer β_1 and β_2 are to 1, the more conformal the contact.

$$R_j = \beta_i r_i \tag{5.2}$$

The stiffnesses for point and quasi-conformal contacts are found to be $250.4 N/mm$ and $1994 N/mm$, respectively. These stiffnesses were then input into the spring system model to find an overall effective stiffness of the device. The stiffness ratios were found between point and conformal configurations and are compared to the experimental values in Table 5.5.

Table 5.5: Stiffness comparison for theoretical (Hertzian) and experimental values.

Axis	Theoretical Point System Stiffness (k_p) [N/mm]	Theoretical Conformal System Stiffness (k_c) [N/mm]	Theoretical Stiffness Ratio (k_c/k_p)	Experimental Stiffness Ratio (k_c/k_p)
x	1002	2996	3.0	---
y	1252	2245	1.8	1.4
z	1753	3246	1.9	1.5

The theoretical stiffness ratios calculated using Hertzian Contact Theory agree with the experimental values within 30%. This indicates that the skin is likely compressed such that the conformal contact does not scale with the stiffness of the skin itself, but with the geometry of the contact relative to the geometry of the head. The initial hypothesis states that using a quasi-conformal contact would greatly improve the stiffness of the complete contact set, because a quasi-conformal contact essentially behaves as a large number of point contacts in series. This method would be advantageous in the case where the stiffness of the contact joint is limited by the compliant nonlinear elastic material—skin. However, from the experimentation and modeling performed in this thesis, it was shown that the stiffness is only improved by a factor of 1-3, compared to the factor of 8-18 initially predicted. The improvement of stiffness is instead largely based upon the increased stiffness due to geometry of the quasi-conformal contact relative to the

head. The theoretical estimates for stiffness ratios are predicted to be higher than the actual measured value because, while the majority of the stiffness is due to the contact stiffness of the geometry, the compliance of the skin is still a relevant factor, and is causes an equal compliance in both systems.

CHAPTER

6

CONCLUSIONS & FUTURE WORK

The purpose of this work was to investigate the modeling and prototyping of quasi-conformal constraints and their application to positioning compliant bodies, such as the holding of mice for optical imaging setups. No existing research has been to systematically investigate quasi-conformal contacts in this application. While some existing methods and positioning devices currently exist, none are able to restrain imaging subjects to the accuracy required. A method for characterizing material properties of nonlinear elastic materials was presented and demonstrated. This information was then used to build a stiffness model for a prototype restraint device which was systematically designed and tested. The performance of the prototype was evaluated and presented.

The direct application of this work is the holding of laboratory mice for biological imaging, particularly bone marrow and brain imaging. To achieve high quality images, the mouse needs to be held such that all movements are less than $1\mu m$. This would allow for better examination and tracking of biological structures, such as stem cells and dendrites, ultimately leading to more discovery in fields such as cancer research and behavioral diseases.

6.1 Thesis Synopsis

Chapter 1 of this thesis presented the background for this work as well as the motivation to develop a restraint device for mice capable of sub-micron performance. Chapter 2 discussed the

design of experiment to characterize mouse facial tissue. The theoretical modeling of quasi-conformal contacts and its integration into a complete device spring system was presented in Chapter 3. The findings from Chapter 2 and 3 were used to design the prototype device, as discussed in Chapter 4. Chapter 5 explained the experimental design, setup, and limitations of the prototype device testing. The results of the experiments were also discussed in this Chapter. It was concluded from this thesis that the stiffness of a quasi-conformal contact on a compliant nonlinear elastic material behaves similarly to a Hertzian contact system and is dependent upon the geometry of the constraint relative to the subject. The remainder of this chapter (Chapter 6) will discuss future work for this research.

6.2 Future Work

While this restraint device was able to minimize momentary anesthetized mouse movement to $<1\mu m$, there are further developments that can be made for this research to create a greater impact. These further developments can be made in a variety of separate directions.

6.2.1 Further Theory Development and Validation

The theoretical modeling for this research can be further refined. The level of conformity of the quasi-conformal contacts can be further characterized. While the contacts in this thesis were examined qualitatively, further measurements and experiments can be performed with various levels of conformity for these contacts to confirm the accuracy of the Hertzian contact theoretical model for this application. Creating a more detailed model would also allow for further optimization of restraint devices for compliant bodies. The effectiveness difference between a truly conformal and quasi-conformal contact can also be investigated. Integrating sensitive electronic pressure sensors can aid in the validation of the effectiveness of these conformal contacts. If the theoretical model can be developed to predict significant improvement of perfectly conformal contacts, a device with truly conformal contacts could be developed with better performance.

6.2.2 Device Refinement

Due to the nature of testing on biological subjects, the testing for this device was fairly limited. Further testing of the device would be beneficial to determine the repeatability of this method. There are several directions in which this research can continue to improve the performance of this device. One direction involves increasing the amount of conformal contact in the device to increase the total stiffness of the device. While the space available to make contact on a mouse head is limited, there are further improvements that can be made.

Another direction involves awake mouse testing. While testing on awake mouse subjects would require more redesign to avoid certain sensitive areas, awake mouse imaging is an extremely valuable field where such a device would allow for further advancements in cancer and behavioral research. Further testing and development in this direction would require further CAC protocol approval.

A slow drift in the data was noticed over long periods of testing. The slow drift was not focused on in this version of the prototype. However, identifying the cause of the slow drift and designing around it can help this device perform fully within the required functional requirements. This prototype device was ultimately designed for testing and modularity, rather than for manufacturing and friendly user-interface. With the current design, many biologists would find the device too cumbersome to use on a daily basis. If the location and design of contacts is validated to be effective, this device could be designed to have good force feedback and easily maneuverable and used for biologists without extra tools required.

6.2.3 Expanding Application for other Medical Imaging

The challenges and requirements for other rodent imaging is similar to those that exist for mice. Details of the prototype device would need to be adjusted, such as device size and geometry, but much of the concepts can be transferred directly to this application. The theory for quasi-conformal and conformal contacts can also be expanded to apply to other types of medical imaging, such as human imaging. Current conformal methods include thermoplastic masks, but these are only able to constrain movements to the order of centimeters. Respiration and muscle

twitches are still a problem for these types of imaging. Further background research to understand the limitations and challenges involved with restraining humans would determine the feasibility of these methods for this application.

REFERENCES

[1] A. H. Slocum, *Precision Machine Design.* Dearborn, Michigan: Society of Manufacturing Engineers, 1992.

[2] "Antique Revival Wooden Kids Seat, Round - Childrens Chairs." [Online]. Available: http://www.amazon.com/Antique-Revival-Wooden-Kids-Round/dp/B007B525OQ. [Accessed: 05-Jan-2016].

[3] "Office Chairs - IKEA." [Online]. Available: http://www.ikea.com/us/en/catalog/categories/departments/workspaces/20652/. [Accessed: 05-Jan-2016].

[4] Y. Wang, K. L. Marshall, Y. Baba, E. A. Lumpkin, and G. J. Gerling, "Compressive Viscoelasticity of Freshly Excised Mouse Skin is Dependent on Specimen Thickness, Strain Level and Rate," *PLoS One*, vol. 10, no. 3, p. e0120897, Jan. 2015.

[5] B. R. Masters and P. T. C. So, "Confocal Microscopy and Multi-photon Excitation Microscopy of Human Skin in Vivo," *Opt. Express*, vol. 8, no. 1, 2001.

[6] D. W. Piston, T. J. Fellers, and M. W. Davidson, "Fundamentals and Applications in Multiphoton Excitation Microscopy," *Nikon Microscopy U.* [Online]. Available: http://www.microscopyu.com/articles/fluorescence/multiphoton/multiphotonintro.html. [Accessed: 05-Jan-2016].

[7] W. Drexler, U. Morgner, F. X. Kärtner, C. Pitris, S. A. Boppart, X. D. Li, E. P. Ippen, and J. G. Fujimoto, "In vivo ultrahigh-resolution optical coherence tomography," *Opt. Lett.*, vol. 24, no. 17, p. 1221, Sep. 1999.

[8] R. Niesner, V. Andresen, J. Neumann, H. Spiecker, and M. Gunzer, "The power of single and multibeam two-photon microscopy for high-resolution and high-speed deep tissue and intravital imaging.," *Biophys. J.*, vol. 93, no. 7, pp. 2519–29, Oct. 2007.

[9] J. Schallek, Y. Geng, H. Nguyen, and D. R. Williams, "Morphology and topography of retinal pericytes in the living mouse retina using in vivo adaptive optics imaging and ex vivo characterization.," *Invest. Ophthalmol. Vis. Sci.*, vol. 54, no. 13, pp. 8237–50, Dec. 2013.

[10] L. R. Ferguson, S. Grover, J. M. Dominguez, S. Balaiya, and K. V Chalam, "Retinal thickness measurement obtained with spectral domain optical coherence tomography assisted optical biopsy accurately correlates with ex vivo histology.," *PLoS One*, vol. 9, no.

10, p. e111203, Jan. 2014.

[11] L. R. Ferguson, S. Balaiya, S. Grover, and K. V Chalam, "Modified protocol for in vivo imaging of wild-type mouse retina with customized miniature spectral domain optical coherence tomography (SD-OCT) device.," *Biol. Proced. Online*, vol. 14, no. 1, p. 9, Jan. 2012.

[12] A. Mizrahi, J. C. Crowley, E. Shtoyerman, and L. C. Katz, "High-resolution in vivo imaging of hippocampal dendrites and spines.," *J. Neurosci.*, vol. 24, no. 13, pp. 3147–51, Mar. 2004.

[13] C. Halin, J. R. Mora, C. Sumen, and U. H. von Andrian, "In vivo imaging of lymphocyte trafficking.," *Annu. Rev. Cell Dev. Biol.*, vol. 21, pp. 581–603, Jan. 2005.

[14] C. Lin and M. L. Culpepper, "Compliant Mouse Restrainer for in vivo Optical Imaging." 2012.

[15] D. P. Holschneider and J.-M. I. Maarek, "Brain maps on the go: functional imaging during motor challenge in animals.," *Methods*, vol. 45, no. 4, pp. 255–61, Aug. 2008.

[16] S. Goel, A. H.-K. Wong, and R. K. Jain, "Vascular normalization as a therapeutic strategy for malignant and nonmalignant disease.," *Cold Spring Harb. Perspect. Med.*, vol. 2, no. 3, p. a006486, Mar. 2012.

[17] D. A. Dombeck, A. N. Khabbaz, F. Collman, T. L. Adelman, and D. W. Tank, "Imaging large-scale neural activity with cellular resolution in awake, mobile mice.," *Neuron*, vol. 56, no. 1, pp. 43–57, Oct. 2007.

[18] R. P. J. Barretto, T. H. Ko, J. C. Jung, T. J. Wang, G. Capps, A. C. Waters, Y. Ziv, A. Attardo, L. Recht, and M. J. Schnitzer, "Time-lapse imaging of disease progression in deep brain areas using fluorescence microendoscopy.," *Nat. Med.*, vol. 17, no. 2, pp. 223–8, Mar. 2011.

[19] H. Mizuma, M. Shukuri, T. Hayashi, Y. Watanabe, and H. Onoe, "Establishment of in vivo brain imaging method in conscious mice.," *J. Nucl. Med.*, vol. 51, no. 7, pp. 1068–75, Jul. 2010.

[20] "Mouse and Neonatal Rat Adaptor - Stereotaxic adaptors - Stereotaxic accessories - Neuroscience." [Online]. Available: http://www.stoeltingco.com/neuroscience/accessories/stereotaxic-adaptors/mouse-and-neonatal-rat-adaptor.html. [Accessed: 05-Jan-2016].

[21] L. Herfst, A. Burgalossi, K. Haskic, J. J. Tukker, M. Schmidt, and M. Brecht, "Friction-based stabilization of juxtacellular recordings in freely moving rats.," *J. Neurophysiol.*, vol. 108, no. 2, pp. 697–707, Jul. 2012.

[22] M. Culpepper, J. Spencer, and C. Lin, "SBIR Proposal: Compliant Mouse Restrainer for in vivo Optical Imaging and Surgery." SBIR Proposal, 2013.

[23] "Do these startling longevity studies mean your lifespan could double?" [Online]. Available: http://io9.gizmodo.com/do-these-startling-animal-studies-mean-your-lifespan-co-486041314. [Accessed: 11-May-2016].

[24] Y. Wang, K. L. Marshall, Y. Baba, G. J. Gerling, and E. a Lumpkin, "Hyperelastic Material Properties of Mouse Skin under Compression.," *PLoS One*, vol. 8, no. 6, p. e67439, Jan. 2013.

[25] B. C. W. Kot, Z. J. Zhang, A. W. C. Lee, V. Y. F. Leung, and S. N. Fu, "Elastic modulus of muscle and tendon with shear wave ultrasound elastography: variations with different technical settings.," *PLoS One*, vol. 7, no. 8, p. e44348, Jan. 2012.

[26] E. J. Chen, J. Novakofski, W. K. Jenkins, and W. D. O'Brien, "Young's modulus measurements of soft tissues with application to elasticity imaging," *IEEE Trans. Ultrason. Ferroelectr. Freq. Control*, vol. 43, no. 1, pp. 191–194, Jan. 1996.

[27] H. Mao, C. Wagner, F. Guan, Y. N. Yeni, and K. H. Yang, "Material Properties of Adult Rat Skull," *J. Mech. Med. Biol.*, vol. 11, no. 05, pp. 1199–1212, Dec. 2011.

[28] R. Dias Carlson, "Precision Constraint of Deformable Bodies for Medical Imaging Applications," Massachusetts Institute of Technology, 2016.

[29] "Air Bushings - English - 0.50 Inch ID | NEWWAY Air bearings." [Online]. Available: http://www.newwayairbearings.com/products/air-bushings-english/air-bushings-english-0.50-inch-id. [Accessed: 16-May-2016].

[30] "TONiC^{TM} encoder series." [Online]. Available: http://www.renishaw.com/en/tonic-encoder-series--37824. [Accessed: 13-May-2016].

[31] "Linear Voice Coil Motor Actuator LVCM-025-029-01, Continuous Force: 18.2 Oz (5.1N), Stroke: 0.63 in (15.9 mm)." [Online]. Available: http://www.moticont.com/lvcm-025-029-01.htm. [Accessed: 13-May-2016].

[32] L. C. Hale, "Principles and Techniques for Designing Precision Machines," 1999.

[33] K. L. Johnson, *Contact Mechanics*. Cambridge, United Kingdom: Cambridge University Press, 1985.

APPENDIX

A

INSTRUMENTATION & ELECTRONICS FOR MATERIALS TESTING

A.1 Instrumentation Setup

The voice coil current control commands were generated and sent using LabVIEW and a NI myRIO. The signal was sent through the amplifier circuit shown in Section A.1.1. The data collected from the Renishaw Linear Encoders were recorded using a NI 9401 Digital I/O module in a DAQ and recorded in LabVIEW as well.

A.1.1 Voice Coil

The PCB layout for the linear voice coil actuator amplifier is shown below in Figure A.1. The power resister R_{sense} was grounded to a large heatsink.

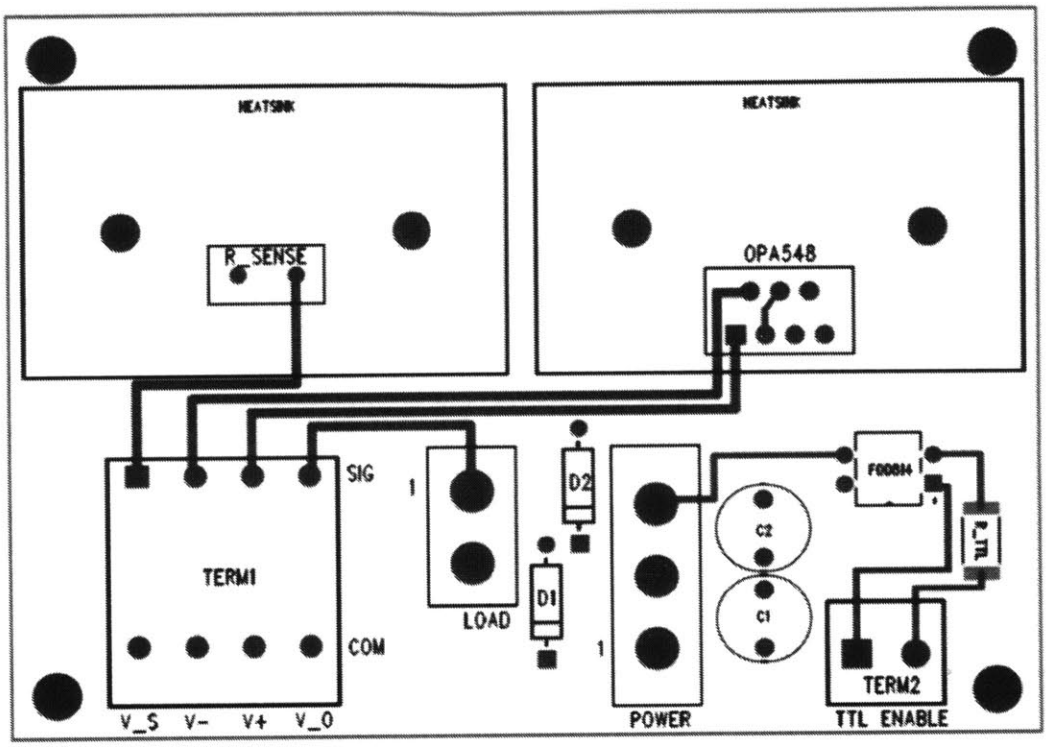

Figure A.1: PCB layout for voice coil control amplifier.

The current control schematic for operating the voice coil is presented in Figure A.2. To convert current load to force, a scaling value given by the voice coil manufacturer was used in Equation (A.1). The scaling value was then verified through testing and calibration.

$$F_{output} = I_{load}(3.75N/A) \tag{A.1}$$

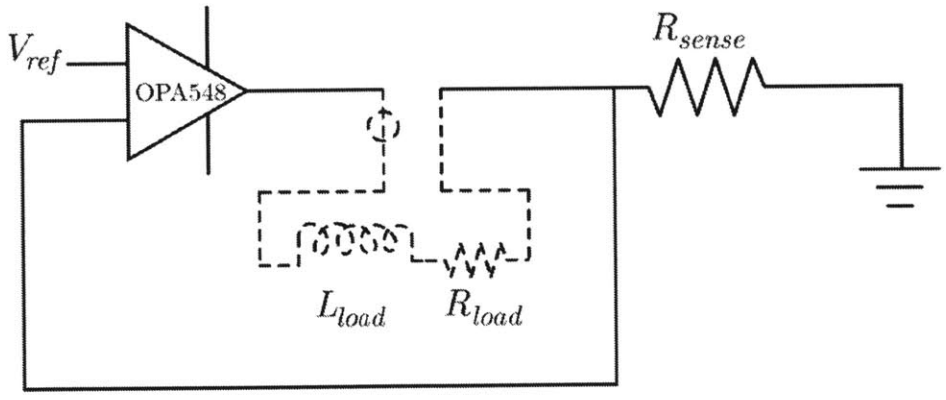

Figure A.2: Current control schematic for voice coil.

The LabVIEW controller supplied a reference voltage V_{ref} set by the user. The relationship between current load and the input reference voltage is shown in Equation (A.2). Equations (A.1) and (A.2) are then combined to find the relationship between output force and input voltage for the control system, shown in Equation (A.3)

$$I_{load} = \frac{V_{ref}}{R_{sense}} \tag{A.2}$$

$$F_{output} = \frac{V_{ref}}{R_{sense}}(3.75N/A) \tag{A.3}$$

APPENDIX

B

ERROR MODEL FOR MATERIALS TESTING SETUP

The overall error model for the materials testing setup described in Chapter 2 is presented in this section. The summary of the possible sources of error and magnitudes are in Table B.1 below.

Table B.1: Error sources for material testing setup.

Error source	Affected Data Variable	x	y	z	Units
Platform Flatness	-	-	-	0.082	μm
Thermal Expansion	δ, x, y	2.5	2.4	2	μm
Flexure Off-axis Travel	-	0.1	-	-	μm
Input Error (δ_y)	δ	-	0.5	-	μm
Encoder Error	x, y	0.0003	0.0003	-	μm
VCA Force Error	F	0.002	-	-	N

The *platform flatness* is dependent on the purchased aluminum baseplate upon which all the components are mounted. Any error in the flatness would be in the z-axis of the device, and therefore does not affect the data collected.

The error due to *thermal expansion* was calculated using thermal expansion coefficients of the bulk materials of individual components and compounded. An assumption of a maximum total temperature change of 1°C was used for this calculation.

Flexure off-axis travel refers to the distance traveled in the constrained degree of freedom of the flexure under applied forces. This value only affects the shear stiffness test and was determined from FEA.

The *input error* for δ refers to the micrometer positioning. This error is due to the limited resolution on the micrometer and how well it was able to be positioned manually; this error is also only relevant to the shear stiffness test.

Encoder error is the accuracy of the Renishaw encoders for the displacement measurements taken for each axis of movement. This is found on the Renishaw data sheets for the encoder.

Voice Coil Actuator (VCA) force error is dependent upon the accuracy of the current-to-force conversion coefficient, the actual resistance of R_{sense}, and the reference voltage. These values were measured empirically.

APPENDIX

C

HERTZIAN CONTACT THEORY

Hertzian contact theory [32] remains the foundation for most contact problems found in engineering. This theory can be applied for normal contact of two smooth and elastic solids with two local radii of curvature. Hertzian contact theory assumes the following about the surfaces involved [33]:

i. The surfaces are continuous and non-conforming

ii. The strains are small

iii. Each solid can be considered as an elastic half-space

iv. The surfaces are frictionless

While ideally conformal contacts are used in this thesis, in a real-world case, the radii of curvature of the mouse head and constraint contact are not exactly the same and are thus considered non-conforming. The strains on the bone and constraint contact are relatively small, as the compression strain of the mouse skin is considered to be maxed out.

The equations for elliptical contacts were used in the calculations of this thesis; this kind of contact forms when two three-dimensional bodies with orthogonal radii of curvature come in contact with each other with force P. The curvature of these bodies can be concave (negative radius of curvature) or convex (positive radius of curvature). Using the major and minor radii of curvature of the two bodies ($R_{1_{xx}}, R_{1_{yy}}, R_{2_{xx}}, R_{2_{yy}}$), the radii of curvature of an equivalent toroid in contact with a plane is found using Equations (C.1)-(C.4) below.

$$R_a = \frac{1}{(A+B)-(B-A)} \tag{C.1}$$

$$R_b = \frac{1}{(A+B)+(B-A)} \tag{C.2}$$

$$A+B = \frac{1}{2}\left(\frac{1}{R_{1_{xx}}} + \frac{1}{R_{1_{yy}}} + \frac{1}{R_{2_{xx}}} + \frac{1}{R_{2_{yy}}}\right) \tag{C.3}$$

$$B-A = \frac{1}{2}\left\{\left(\frac{1}{R_{1_{xx}}} - \frac{1}{R_{1_{yy}}}\right)^2 + \left(\frac{1}{R_{2_{xx}}} - \frac{1}{R_{2_{yy}}}\right)^2 \ldots + 2\left(\frac{1}{R_{1_{xx}}} - \frac{1}{R_{1_{yy}}}\right)\left(\frac{1}{R_{2_{xx}}} - \frac{1}{R_{2_{yy}}}\right)\cos(2\alpha)\right\}^{\frac{1}{2}} \tag{C.4}$$

A first order approximation of the radius of an equivalent sphere in contact with a plane is then calculated in Equation (C.5): R_c.

$$R_c = \sqrt{R_a R_b} \tag{C.5}$$

The approximate eccentricity of the contact ellipse is then calculated in Equation (C.6)

$$e^2 = 1 - \left(\frac{b}{a}\right)^2 \cong 1 - \left(\frac{R_b}{R_a}\right)^{\frac{4}{3}} \tag{C.6}$$

The radius of an equivalent circle of contact, c, is calculated with a correction factor F_1; the calculation for the radius is shown in (C.7) and the curve fit for the correction factor is shown in Equation (C.12).

$$c = \sqrt{ab} = \left(\frac{3PR_c}{4E_c}\right)^{\frac{1}{3}} F_1 \tag{C.7}$$

The major and minor contact radii, a and b, can then be found using Equations (C.8) and (C.9).

$$a = c(1 - e^2)^{-\frac{1}{4}} \tag{C.8}$$

$$b = c(1 - e^2)^{\frac{1}{4}} \tag{C.9}$$

The normal displacement (δ) and stiffness (k) of the contact joint are then found using Equations (C.10) and (C.11), respectively.

$$\delta = \frac{c^2 F_2}{R_c F_1^2} = \frac{abF_2}{R_c F_1^2} \tag{C.10}$$

$$k = \frac{2E_c c}{F_1 F_2} \tag{C.11}$$

The curve fit values of the correction factors F_1 and F_2 are shown below in Equations (C.12) and (C.13).

$$F_1 \cong 1 - \left[\left(\frac{R_a}{R_b}\right)^{0.0602} - 1\right]^{1.456} \tag{C.12}$$

$$F_1 \cong 1 - \left[\left(\frac{R_a}{R_b}\right)^{0.0684} - 1\right]^{1.531} \tag{C.13}$$